arXiv:1504.03236v2 [astro-ph.GA] 16 Jul 2015

A WARP IN PROGRESS: H I AND RADIO CONTINUUM OBSERVATIONS OF THE SPIRAL NGC 3145

Michele Kaufman[1], Elias Brinks[2], Curtis Struck[3], Bruce G. Elmegreen[4],
and Debra M. Elmegreen[5]

Draft version July 17, 2015

ABSTRACT

VLA H I observations and $\lambda 6$ cm radio continuum observations are presented of the barred-spiral galaxy NGC 3145. In optical images NGC 3145 has stellar arms that appear to cross, forming "X"-features. Our radio continuum observations rule out shock fronts at three of the four "X" features, and our H I data provide evidence of gas motions perpendicular to the disk of NGC 3145. In large portions of NGC 3145, particularly in the middle-to-outer disk, the H I line-profiles are skewed. Relative to the disk, the gas in the skewed wing of the line-profiles has z-motions away from us on the approaching side of the galaxy and z-motions of about the same magnitude (~ 40 km s^{-1}) toward us on the receding side. These warping motions imply that there has been a perturbation with a sizeable component perpendicular to the disk over large spatial scales. Two features in NGC 3145 have velocities indicating that they are out-of-plane tidal arms. One is an apparent branch of a main spiral arm on the northeastern side of NGC 3145; the velocity of the branch is ~ 150 km s^{-1} greater than the spiral arm where they appear to intersect in projection. The other is the arm on the southwestern side that forms three of the "X"-features. It differs in velocity by ~ 56 km s^{-1} from that of the disk at the same projected location. H I observations are presented also of the two small companions NGC 3143 and PGC 029578. Based on its properties (enhanced SFR, H I emission 50% more extended on its northeastern side, etc.), NGC 3143 is the more likely of the two companions to have interacted with NGC 3145 recently. A simple analytic model demonstrates that an encounter between NGC 3143 and NGC 3145 is a plausible explanation for the observed warping motions in NGC 3145.

Subject headings: galaxies: individual (NGC 3145, NGC 3143, PGC 029578) - galaxies: interactions - galaxies: ISM - galaxies: kinematics and dynamics - radio continuum: galaxies

1. INTRODUCTION

NGC 3145 at a distance of 54.8 Mpc is a barred spiral galaxy with grand-design spiral arms and some peculiar stellar morphology. In the Hubble Atlas of Galaxies, Sandage (1961) writes about NGC 3145 "There is a single faint arm in the southwest quadrant which crosses one of the regular arms nearly at right angles. This is a very rare feature of galaxies ..." We were intrigued by this description and by the presence of three additional places where stellar arms also appear to cross, forming "X"-features, in NGC 3145. The goal of this paper is to understand these puzzling features by investigating what is happening in the interstellar gas at the "X"-features and elsewhere in the galaxy.

NGC 3145 has two smaller companions: the barred spiral NGC 3143 and the Sdm galaxy PGC 029578. We refer to these three galaxies as the NGC 3145 triplet.

The top panel in Figure 1 displays a B-band image of NGC 3145 with some of the optical oddities marked,

[1] 110 Westchester Rd, Newton, MA 02458; email: kaufmanrallis@icloud.com
[2] University of Hertfordshire, Centre for Astrophysics Research, College Lane, Hatfield AL10 9AB, UK; email: E.Brinks@herts.ac.uk
[3] Department of Physics and Astronomy, Iowa State University, Ames, IA 50011; email: curt@iastate.edu
[4] IBM Research Division, T.J. Watson Research Center, 1101 Kitchawan Rd., Yorktown Heights, NY 10598; email: bge@us.ibm.com
[5] Department of Physics and Astronomy, Vassar College, 124 Raymond Av., Poughkeepsie, NY 12604; email: elmegreen@vassar.edu
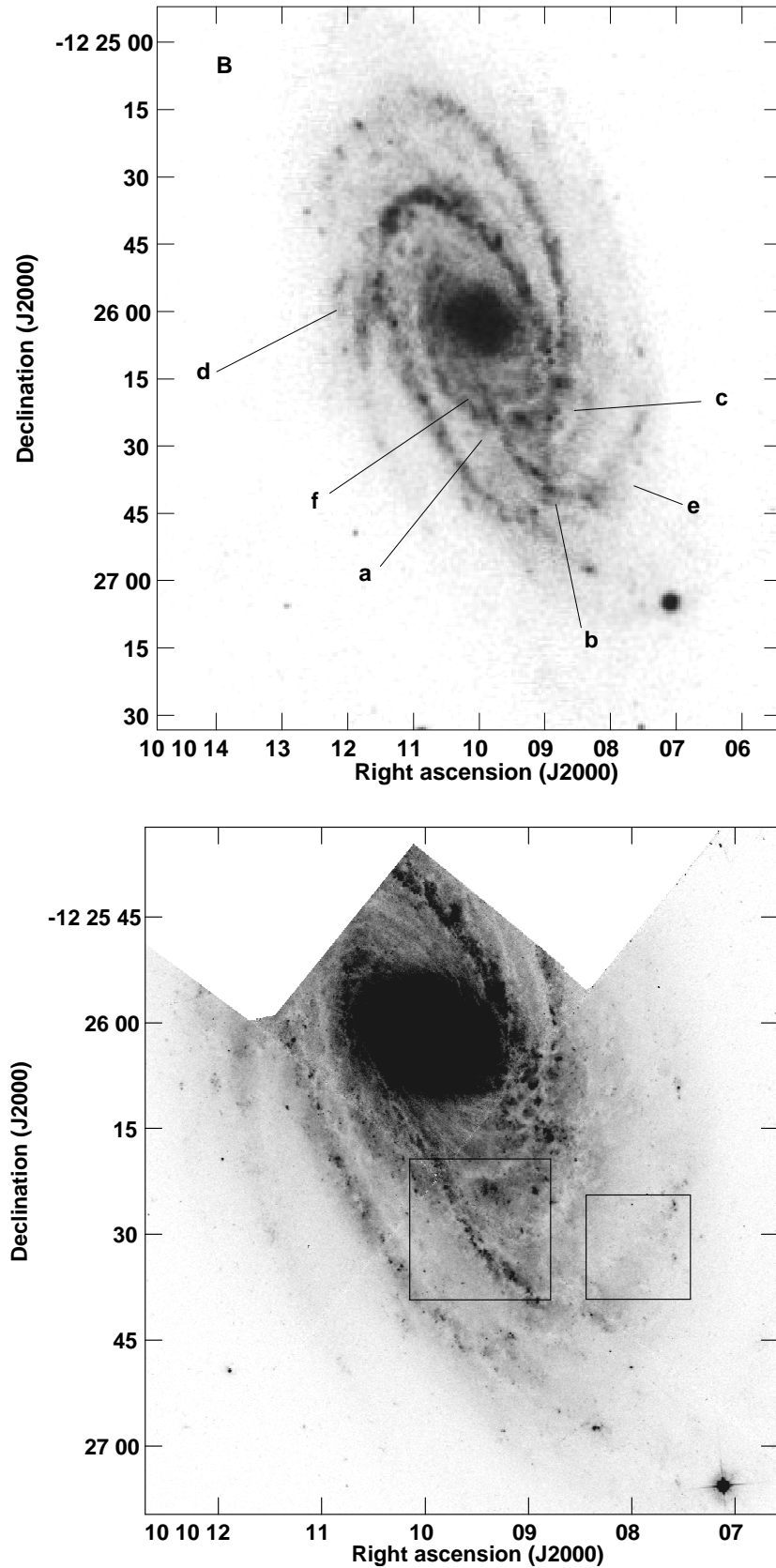
and the bottom panel displays the *Hubble Space Telescope* (HST) R-band image of the southern half of this galaxy. On the southern side of the galaxy, arms cross and outline an apparent optical triangle with base 12″, height 15″, and apices labelled a (the eastern apex), b (the southern apex), and c (the western apex). We refer below to this feature as the *triangle*. Sandage's peculiar arm outlines the eastern edge of the *triangle*. It crosses the inner spiral arm, forming an "X"-feature at apex a; at apex b it produces another "X"-feature. At the location marked f in Figure 1, it creates what looks like another "X"-feature. The inner spiral arm, which has a major dust lane along its concave side, outlines the northern edge of the *triangle*, connecting apices a and c. Another arm connects apices b and c to form the western edge of the *triangle*. At apex b it meets Sandage's peculiar arm. Southward of apex b the two arms diverge, and Sandage's peculiar arm extends to the west. We call the latter the western antenna and label it e in this Figure. On the northeastern side of NGC 3145, we label as Feature d the location where a feature that optically looks like a spiral-arm branch departs from the main spiral arm. We shall refer to this as the *branch* even though the data presented here suggest that it is a tidal arm.

In his study of caustic waveforms in two dimensions, Struck-Marcell (1990) notes that the *triangle* in NGC 3145 resembles a swallowtail caustic. In a swallowtail caustic, five intersecting star streams create a triangular region outlined by arms plus two thin antennae emerging from one of the triangle's vertices. In his study, swallowtail caustics develop within expanding pseudo-rings.

Figure 1. Top: *B* image of NGC 3145 with some optical anomalies marked, e.g. "X"-features where arms appear to cross at apices *a*, *b*, and *c* of the *triangle* and at location *f*. Sandage's peculiar arm outlines the eastern edge of the *triangle* from apex *a* to apex *b*. The apparent *branch* of a main spiral arm is labelled *d*, and the western antenna is labelled *e*. Bottom: *HST* WFPC2 *R* image of NGC 3145. H I line-profiles for the regions enclosed by the boxes will be displayed and discussed in Section 4.

Gas streams do not pass through each other without colliding and shocking. To study the above optical anomalies and look for other unusual features in the gas, we made Karl G. Jansky Very Large Array (VLA)[6] H I observations of the NGC 3145 triplet and $\lambda 6$ cm radio continuum observations of NGC 3145. We use the radio continuum image to check on whether there are strong shock fronts at the "X"-features as would be expected if the intersecting arms are in the same plane.

The purpose of the H I data is to look for evidence of gas flows in extra-planar gas and gas flows perpendicular to the disk over large spatial scales, e.g., are there multiple components in the H I line profiles. For edge-on galaxies displacements above the disk would be obvious. Since the inclination i of NGC 3145 is $50° - 55°$, we get only indirect information.

NGC 3145 is one of the 11 galaxies in the seminal study by Rubin et al. (1978) on extended rotation curves of high-luminosity spiral galaxies. Rubin et al. (1982) include NGC 3145 in their study of the rotational properties of Sb/bc galaxies from optical observations of the rotation curves along the major axis. Their data are used by Persic & Salucci (1991) in fitting a universal rotation curve to spiral galaxies. Our H I observations are the first determination of the velocity field image of NGC 3145 and the kinematic parameters derived from it. It is important to know if gas flows perpendicular to the disk have a significant effect on its rotation curve.

From the NASA/IPAC Extragalactic Database (NED), we adopt a redshift-based distance for NGC 3145 of 54.8 Mpc, which is cosmology-corrected to the 3 K microwave background reference frame with $H_0 = 73$ kpc s^{-1} Mpc^{-1}, $\Omega_m = 0.27$, and $\Omega_\lambda = 0.73$. Then $1'' = 262$ pc.

Table 1 lists basic optical and near-infrared properties of the NGC 3145 triplet from the NASA/IPAC Extragalactic Database and includes data from the Third Reference Catalogue (de Vaucouleurs et al. 1991) and from the Two Micron All Sky Survey (*2MASS*) (Skrutskie et al. 2006). In the literature, there is not very much data about the two companions, and the determination of their systemic velocities has had a checkered history. Our H I observations resolve the issues about the systemic velocities of the companions and provide values of their H I masses. Our velocity field image of PGC 029578 allows us to calculate its dynamical mass.

All of the velocities listed in this paper are heliocentric and use the optical definition of the nonrelativistic Doppler shift.

Section 2 describes our VLA observations, data reduction, and additional images used in this paper. Section 3 discusses the broad-band optical, Hα, radio continuum, and infrared properties of NGC 3145. Section 4 presents the H I properties of NGC 3145. Section 5 presents our H I results on the two companions. Section 6 summarizes and discusses our conclusions. A simple analytic model for the encounter is given in the Appendix.

2. OBSERVATIONS AND DATA REDUCTION

2.1. *H I Observations*

We observed the NGC 3145 triplet in H I at the VLA for 4.75 hr (on target) in C configuration on 1993 July 16 and for 1 hr in D configuration on 1993 October 31. The phase calibrator was 0941-080. For the D configuration observations 3C 286 served as the flux standard and bandpass calibrator. For the C configuration observations 3C 48 and 3C 286 were the flux standards and bandpass calibrators. The phase center was R.A., decl. (2000) = 10 10 06.915, -12 29 46.80. We used on-line Hanning smoothing. H I emission is present for heliocentric velocities 3407 to 3919 km s^{-1}.

For the correlator mode, we adopted the same type of 4IF (intermediate frequency) mode used by Elmegreen et al. (1995) for H I observations of NGC 2207/IC 2163. Thus we made simultaneously (a) observations with a channel width of 21.13 km s^{-1} in IFC and IFD (left circular polarization) and (b) observations with a channel width of 5.28 km s^{-1} in IFA and IFB (right circular polarization). The line-free channels of the data taken with 21.13 km s^{-1} velocity resolution provide the continuum to subtract from the higher velocity-resolution data. The latter had no line-free channels at the low frequency end and only a short range of line-free channels at the high frequency end. In retrospect, this was not the best choice of correlator mode for the NGC 3145 observations because of beam squint, as explained below.

The AIPS software package was used for the data reduction and analysis. The 4 IFs plus two configurations resulted in 8 uv data sets. In each of these, two channels suffered radio frequency interference (RFI) which occurred at different frequencies in the various data sets. To correct for this, we made a continuum image from the line-free channels of IFC and IFD and subtracted the clean components of the brighter continuum sources from every channel in each of the 8 uv data sets. Then for the channels affected by RFI, we interactively clipped any signal above 1 to 2 Jy.

For each uv data set separately, we generated "dirty" data cubes of line plus residual continuum emission, subtracted the residual continuum obtained from IFC and IFD, and cleaned the cubes. Then combining the data from C and D configurations, we repeated the mapping and cleaning and merged the IFs to create one cube with 21.13 km s^{-1} velocity resolution and one with 5.28 km s^{-1} velocity resolution. After inspection, we decided to omit the 5.28 km s^{-1} velocity resolution data taken with D configuration because beam squint, i.e., a slight difference in pointing between the left and right polarization detectors, caused a problem for the D-configuration data when the continuum derived from IFC plus IFD was subtracted from the observations made with IFA and IFB. Since beam squint is less of a problem for C-configuration, we kept the C-configuration data cubes with 5.28 km s^{-1} velocity resolution, but to increase the S/N we averaged the channels to 10.57 km s^{-1} velocity resolution.

To select areas of genuine H I emission, we convolved the cube made with natural weight and 21.1 km s^{-1} channels to $60''$ resolution, clipped it at 2.5 times its rms noise, and retained regions of emission only if the feature appeared in at least two adjacent velocity channels. The resulting cube was applied as a blanking mask to

Table 1
Basic Optical and Near-Infrared Data on the NGC 3145 Triplet[a]

Characteristic	NGC 3145	NGC 3143	PGC 029578
Morphological type	SB(rs)bc	SB(s)b	Sdm
Right ascension (J2000)	$10^h 10^m 09\overset{s}{.}869$	$10^h 10^m 03\overset{s}{.}98$	$10^h 10^m 02\overset{s}{.}32$
Declination (J2000)	$-12°26'01\overset{''}{.}6$	$-12°34'52\overset{''}{.}9$	$-12°38'51\overset{''}{.}6$
$v_{\rm sys}$(helio) (km s^{-1})	3652 ± 6	3536	3586 ± 30
Isophotal major diameter D_{25}	$194'' \pm 13''$	$52'' \pm 8.7''$	$102'' \pm 16.6''$
D_{25} diameter (kpc)	51	14	27
B_T (RC3) (mag) [b]	12.54 ± 0.13	14.9 ± 0.20	$\cdots$
Corrected B_T^0	11.82	14.46	$\cdots$
Galactic A_B	0.234	0.244	0.25
M_B (mag)	-21.87	-19.2	$\cdots$
B (Fick Obs.) (mag)[b]	$\cdots$	15.2	16.6
R (Fick Obs.) (mag)[b]	$\cdots$	13.7	15.3
$(B-V)_T^0$	0.63	0.50	$\cdots$
$(K_s)_{\rm total}$ (mag)	8.62 ± 0.029	11.46 ± 0.11	$\cdots$
$J_{\rm total}$	9.59 ± 0.017	12.20 ± 0.05	$\cdots$
i from axis ratio	55°	35°	68°
Major Axis PA from K_s	205°	225°	$\cdots$
Projected separation from NGC 3145 (kpc)	0	141	204
Distance (Mpc)	54.8	54.8	54.8
Scale (pc per 1$''$)	262	262	262

[a] v_{sys} of PGC 029578 from Zaritsky et al. (1997) (but is not consistent with our HI value) and v_{sys} of NGC 3143 from Schweizer (1987). Aside from the Fick observatory values of B and R for the companions, the rest of the data are from de Vaucouleurs et al. (1991) or 2MASS
[b] Not corrected for extinction

Table 2
Final H I Subcubes

Parameter	Cube 1	Cube 2	Cube 3	Cube 4
Configuration	C + D	C + D	C	C
Channel width (km s^{-1})	21.13	21.13	10.57	5.28
Weighting	Natural	Robust 0.1	Natural	Natural
PSF (FWHM, PA)	$30\overset{''}{.}6 \times 18\overset{''}{.}4, -31°$	$22\overset{''}{.}0 \times 14\overset{''}{.}7, -28°$	$27\overset{''}{.}3 \times 16\overset{''}{.}6, -29°$	$27\overset{''}{.}3 \times 16\overset{''}{.}6, -29°$
Pixel Size	5$''$	5$''$	5$''$	5$''$
Number of channels	32	32	52	104
T_b/I (K/mJy beam^{-1})	1.10	1.92	1.37	1.37
$\sigma_{\rm rms}$ (mJy beam^{-1})[a]	0.50	0.58	0.74	1.04

[a] rms noise per channel

the other cubes. Table 2 lists properties of our four final H I data subcubes. The one with highest sensitivity is Cube 1, made from C plus D configuration data with natural weighting and 21.1 km s^{-1} velocity resolution. The one with highest spatial resolution is Cube 2, made from C plus D configuration data with Robust = 0.1 in the AIPS task IMAGR and 21.1 km s^{-1} velocity resolution. The cube with highest velocity-resolution (and the largest rms noise) is Cube 4 made from C configuration data alone with natural weighting and 5.28 km s^{-1} velocity resolution. Cube 3 was made from Cube 4 by averaging the channels to 10.57 km s^{-1} velocity resolution to reduce the rms noise.

For the line-of-sight H I column density image displayed in the figures below, we convolved the zeroth moment image made from Cube 2 to a circular 22$''$ (HPBW) beam and corrected for primary-beam attentuation. This correction factor has a mean value of 1.04 at the location of NGC 3145, 1.07 at the location of NGC 3143, and 1.26 at the location of PGC 029578.

For NGC 3145, we find the integrated H I line flux S(HI) is 20.4 Jy km s^{-1}, which corresponds to an H I mass M(HI) of 1.4×10^{10} $M_\odot$. Our value of S(HI) for NGC 3145 is 30% greater than the H I Parkes All Sky Survey value (Doyle et al. 2005) of 15.4 Jy km s^{-1}. For NGC 3143, we find S(HI) is 0.91 Jy km s^{-1}, and thus M(HI) $= 6.5 \times 10^8$ $M_\odot$. As we shall see below, NGC 3143 is somewhat deficient in H I. For PGC 029578, we find S(HI) is 4.7 Jy km s^{-1}, and thus M(HI) $= 3.3 \times 10^9$ $M_\odot$.

2.2. Radio Continuum Observations at λ6 cm

With the VLA, we observed NGC 3145 in the radio continuum at a central frequency of 4860.1 MHz for 1 hr (on target) in C configuration on 1994 October 21 and for 48 min in D configuration on 1995 May 13. The observations were made with one IF pair at 4885.1 MHz and the other at 4835.1 MHz, each with a 50 MHz bandwidth. The phase center was R.A., decl.(2000) = 10 10 09.995, -12 26 01.90, within 2$''$ of the NGC 3145 nucleus. The phase calibrator was 0941-080, and the flux calibrator was 3C 286. The smaller galaxies NGC 3143 and PGC 029578 were too far from the phase center to be detected.

Table 3
Resolution of Images[a]

Image	FWHM of PSF
Carnegie Atlas of Galaxies B	$1.3'' \times 1.2''$
MDM B	$2.3'' \times 1.9''$
MDM V	$1.9'' \times 1.6''$
MDM R	$1.7'' \times 1.5''$
Burrell-Schmidt B	$4.1''$
HST WFPC2 R	$0.20'' \times 0.18''$
DSS IIIaJ	$5.4'' \times 4.4''$
Hα	$\sim 1''$
$\lambda 6$ cm radio continuum	$7.4'' \times 5.5''$
$\lambda 6$ cm radio continuum	$7.5''$
N(HI)	$22''$
WISE 12 μm	$9.2'' \times 8.4''$
WISE 22 μm	$18'' \times 17''$

[a] Except in the case of the radio images and the Hα image, the FWHM values are from fitting two-dimensional Gaussians to stellar images in the optical or WISE 3.4 μm image. For the Hα image, we list the value of the estimated seeing from Banfi et al. (1993).

The AIPS software was used for the data reduction. After calibrating the uv data from each VLA configuration separately and checking the separate maps, we combined the uv data from the two configurations and ran the AIPS task IMAGR with ROBUST = 0 to make and clean a map with synthesized beam $7.4'' \times 5.5''$ (HPBW) and BPA = $12°$. A surface brightness of 1 mJy beam^{-1} corresponds to $T_b = 1.275$ K, and the rms noise $\sigma_{\rm rms}$ is 0.0224 mJy beam^{-1}, equivalent to $T_b = 0.029$ K. The mean correction for primary beam attenuation in NGC 3145 is a factor of 1.009. We also convolved this image to a circular beam of $7.5''$ (HPBW). In this image, displayed in the figures below, a surface brightness of 1 mJy beam^{-1} corresponds to $T_b = 0.920$ K and the rms noise is 0.0228 mJy beam^{-1}, equivalent to $T_b = 0.021$ K. For NGC 3145 we find a total flux density $S_\nu(4.86 \text{ GHz}) = 9.1 \pm 0.3$ mJy.

2.3. *Additional Data*

We use Hα, broad-band optical, and infrared images that other observers and facilities have made available on-line. Table 3 lists the FWHM of the point-spread functions (PSFs) of these images. The continuum-subtracted Hα image of NGC 3145 is from Banfi et al. (1993) and is not flux-calibrated. The B image in Figure 1 is from Sandage & Bedke (1994). Whenever we refer to a B image of NGC 3145 without further specification, we mean this image. We use the other B images described below when we need a larger field. We obtained a WFPC2, F606W (R-band) Hubble Space Telescope (*HST*) image from the *Hubble Legacy Archive*[7]. Martini et al. (2003) made these *HST* observations to study circumnuclear dust, but in addition to the central regions, the field covers the southern half of NGC 3145.

We obtained from the NASA/IPAC Infrared Science Archive infrared images of NGC 3145 taken by the Wide-field Infrared Survey Explorer (*WISE*). We also use data from *2MASS*.

Paul Eskridge took B, V, and R images of NGC 3145 for us at the 1.3 m telescope of the Michigan-Dartmouth-M.I.T. Observatory (MDM) on 1999 March 25. These images, taken under non-photometric conditions, are a little trailed and a little underexposed. We took a B image with the Burrell-Schmidt telescope at Kitt Peak on 1993 January 29 and use this for NGC 3143. These images were bias subtracted, flat-fielded, combined, and sky-subtracted with standard IRAF procedures.

For PGC 029578 we use a IIIaJ (4680 Å) Digitized Sky Survey (DSS) image from Space Telescope Science Institute.

Philip Appleton took B and R images for us of NGC 3143 and PGC 020578 at the 0.6 m telescope of the Fick Observatory of Iowa State University, and he measured the (Johnson) B and R magnitudes listed in Table 1 for these two galaxies.

3. BROAD-BAND OPTICAL, Hα, RADIO CONTINUUM, AND INFRARED PROPERTIES OF NGC 3145

Throughout this section we use for deprojection of NGC 3145 the values of the position angle (PA) of the major axis and the inclination i of the disk from Table 1. Our H I kinematic data in Section 4.2 find a value for the major axis PA consistent with the isophotal value in this table and a somewhat smaller value of i.

3.1. *Broad-band Optical*

The *HST* R-band image of the southern half of NGC 3145, displayed in the bottom panel of Figure 1, affords a detailed view of some of the optical oddities marked in the top panel of that figure. The larger box encloses the *triangle*, and the smaller box is on the western antenna. Sets of H I line-profiles from these two boxes will be displayed and discussed in Section 4.2.2. Heading north from apex c of the *triangle* is a region of complex dust loops and feathers. *HST* images of Sb and Sc galaxies often reveal dust feathers crossing spiral arms (La Vigne et al. 2006). Numerical models of spiral galaxies by Kim & Ostriker (2002), Kim & Ostriker (2006), and Shetty & Ostriker (2006) reproduce feathers and spurs as sheared structures resulting from magneto-Jeans instabilities as gas flows through a spiral shock, and Lee & Shu (2012) and Lee (2014) present an analytic discussion of the feathering instability of spiral arms for a thin disk with magnetic fields and self-gravitating gas. The dust feathers in this region of NGC 3145 are spaced 0.3 to 0.7 kpc apart and are probably produced by this mechanism. It is not clear whether this mechanism accounts for the dust loops in this part of NGC 3145. We shall refer to this region as the region of complex dust loops.

Sandage's peculiar arm, which outlines the eastern edge of the *triangle*, is prominent in the HST image. Crossed by a number of dust feathers, it has a dust lane along part of its outer edge and another along part of its inner edge. This arm looks to be in front of the inner spiral arm, which it crosses at apex a, and thus in front of the disk. Figure 2 is a display of the B image in polar coordinates after deprojection into the plane of
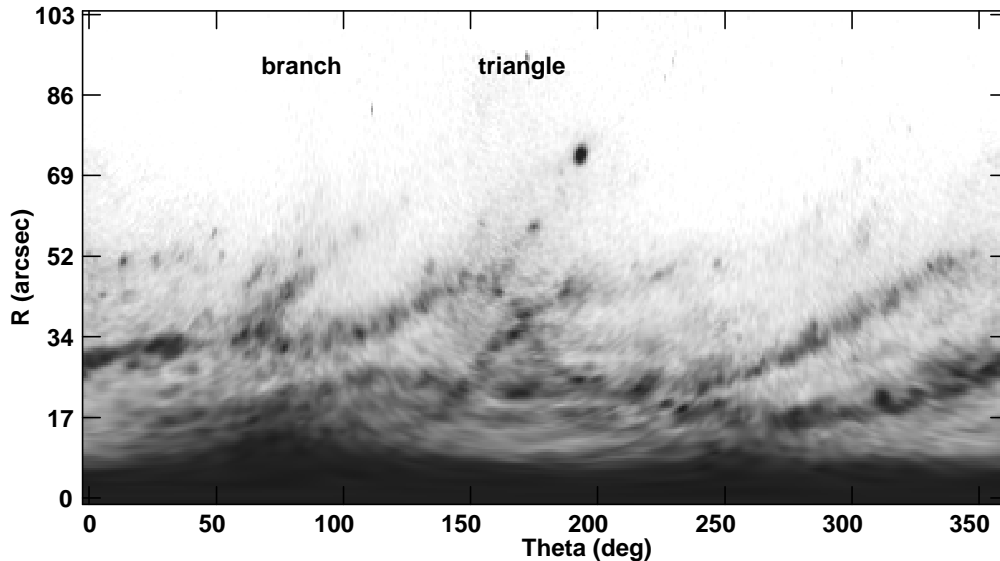
Figure 2. Greyscale polar coordinate display of the B image of Figure 1 after deprojection into the plane of NGC 3145. The azimuth θ is measured ccw from the NNE major axis. Some notable features are the *triangle* and the apparent *branch* of the main spiral arm starting at Feature d, as marked in Figure 1. The labels "branch" and "triangle" indicate the approximate values of θ for these features. Apex a of the *triangle* has $\theta \simeq 146°$. The arm connecting apices b and c of the *triangle* winds in opposite sense to all the other arms.

NGC 3145. In this image, the *triangle* is a prominent feature, and Sandage's peculiar arm has quite a different slope than the spiral arms, consistent with it being a material arm in front of the disk. The *branch* starting at Feature d is also visible in this image. Its slope in this polar-coordinate diagram is about the same as that of Sandage's peculiar arm between apices a and b.

The arm which outlines the western edge of the *triangle* and connects apices c and b winds in opposite sense to every other arm in NGC 3145 (see Figures 1 and 2); it increases in radius cw whereas all the other arms increase in radius ccw. It is less prominent in the R-band HST image than in the B image of Figures 1 and 2. In our MDM images of NGC 3145, this arm decreases in prominence from B to V to R. This suggests it is dominated in B by somewhat younger stars.

In Figure 1 there is also a string of bluish clumps crossing Sandage's peculiar arm at Feature f ($6''$ north of apex a) and continuing, quasi-parallel to the northern edge of the *triangle*, to the southern part of the region of compex dust loops. This string of clumps is not evident in the HST image.

From *2MASS* K_s isophotes, the position angle (PA) of the major axis of the bar is $60°$. The region of complex dust loops and the location where the *branch* (feature d in Figure 1) departs from the spiral arm are on opposite sides of the galaxy at somewhat different distances from the nucleus and roughly along the same PA as the major axis of the bar.

3.2. *Radio Continuum, Hα, and mid-IR*

For NGC 3145, the NRAO/VLA Sky Survey (NVSS) (Condon et al. 1998) lists a total flux density $S_\nu(1.4$ GHz) of 21.5 ± 2.3 mJy. Since we find $S_\nu(4.86$ GHz) $= 9.1 \pm 0.3$ mJy, the global spectral index α of NGC $3145 = -0.7 \pm 0.1$, which is typical of normal spirals. For normal galaxies with a spectal index in this range, the expression in Condon (1992) for the ratio of free-free to total flux density gives a thermal fraction at $\lambda 6$ cm

for a galaxy as a whole of 20% to 25%.

Usually in spiral galaxies, the extended emission along the spiral arms is predominantly nonthermal, and only where knots occur is the emission mainly free-free. Young star-forming complexes appear as Hα sources and knots of $\lambda 6$ cm radio continuum emission in NGC 3145. The $\lambda 6$ cm radio continuum is also used to search for possible shock fronts. The left panel in Figure 3 displays in greyscale and contours the $\lambda 6$ cm radio continuum image with $7.5''$ ($= 2.0$ kpc) resolution. In the right panel, these contours are overlaid on a greyscale display of the Hα image (which has a resolution of $\sim 1'' = 260$ pc). In Figure 4, the $\lambda 6$ cm contours are overlaid on the B image in greyscale to show where the radio continuum emission is located relative to the features marked in Figure 1.

The $\lambda 6$ cm knots tend to lie along the brighter parts of the B-band spiral arms, and several coincide with Hα clumps, but not all of the brighter Hα clumps are seen as $\lambda 6$ cm emission knots.

The two brightest $\lambda 6$ cm clumps lie on the inner and brighter of the two B-band spiral arms in the north and have flux densities $S_\nu(6$ cm) $= 0.44 \pm 0.04$ mJy for the northwestern clump and 0.41 ± 0.04 mJy for the northern clump. Neither of these is at the "X"-features marked in Figure 1.

In Figure 5, contours from our $\lambda 6$ cm radio continuum image with higher resolution ($7.4'' \times 5.5''$ HPBW) are overlaid on the portion of the HST image containing the region of complex dust loops. This region has $\lambda 6$ cm flux density $S_\nu(6$ cm) $= 0.73 \pm 0.06$ mJy. Although there is Hα emission here, some of the extended $\lambda 6$ cm emission may be from shocks associated with the dust loops and feathers. The $\lambda 6$ cm clump centered where a large dust loop or shell seems to cross another feature here has $S_\nu(6$ cm) $= 0.21 \pm 0.03$ mJy.

The following properties of Sandage's peculiar arm, the *triangle*, and the "X"-features are apparent from a comparison of Figures 3, 4, and 1. There is a radio continuum knot at Feature f (labelled in Figure 3), which
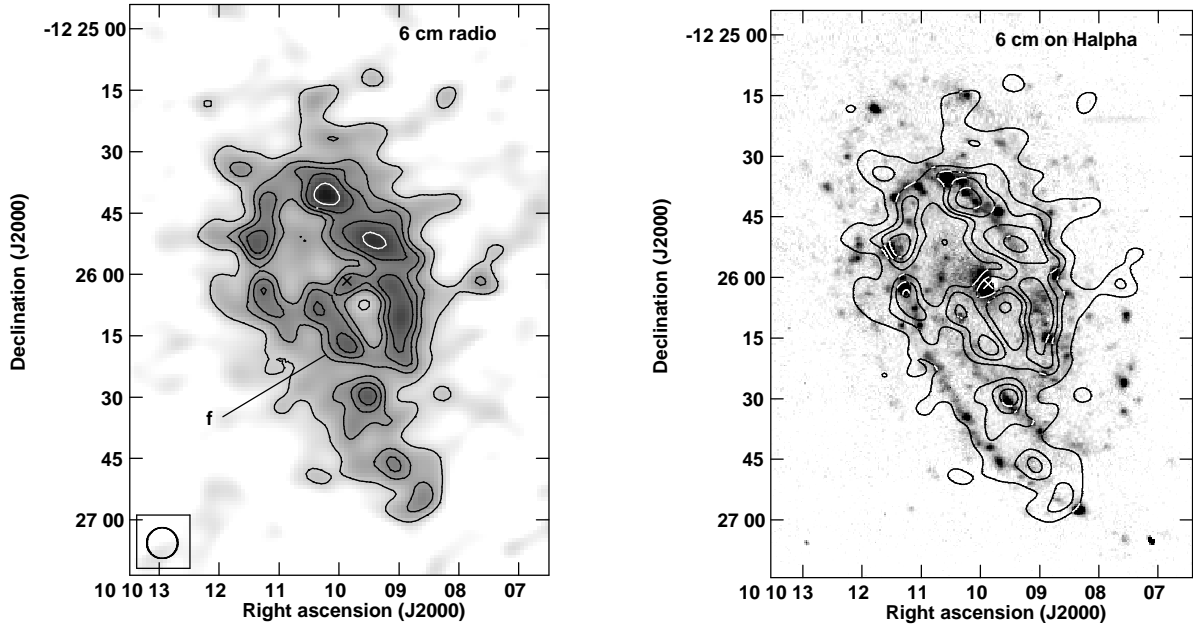
Figure 3. Left: Greyscale plus contour display of the $\lambda 6$ cm radio continuum image of NGC 3145 with 7.5″ resolution. Contour levels are at (3, 5, 6, 7, 9) × the rms noise. The rms noise is 0.0228 mJy beam^{-1}, equivalent to $T_b = 0.021$ K. See text about Feature f. Right: Greyscale display of Hα image overlaid with contours of $\lambda 6$ cm radio continuum emission. Several of the $\lambda 6$ cm radio knots coincide with Hα clumps. The cross marks the location of the nucleus.
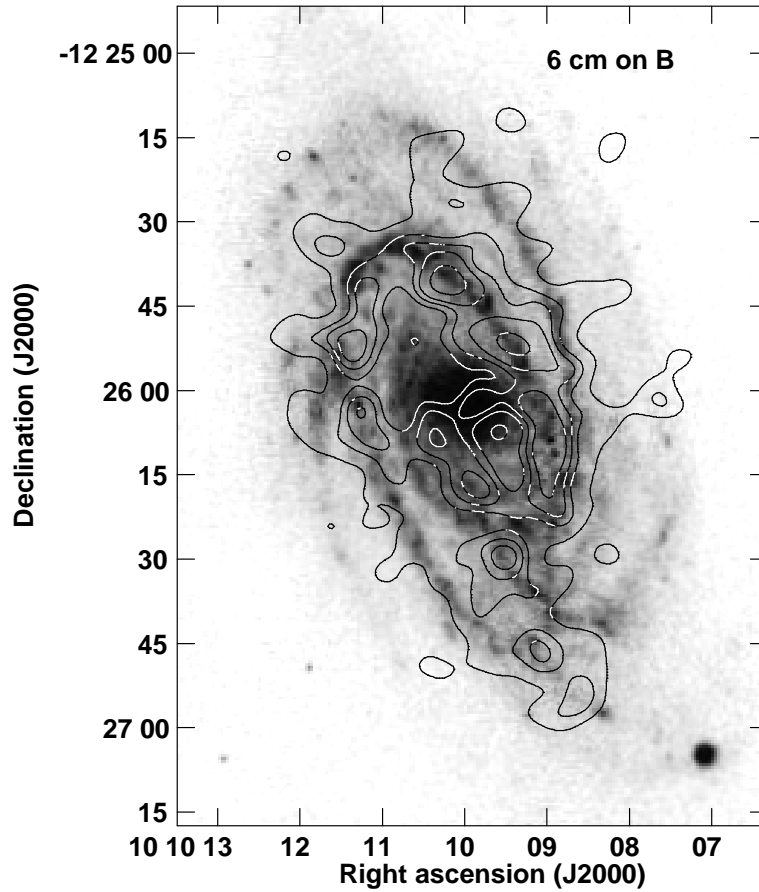

Figure 4. Greyscale display of B image of NGC 3145 overlaid with contours of $\lambda 6$ cm radio emission from Figure 3. *Apices a and b of the triangle are not prominent in the $\lambda 6$ cm radio.* North of Feature f (marked in Figure 3) there is extended $\lambda 6$ cm radio emission along Sandage's peculiar arm.
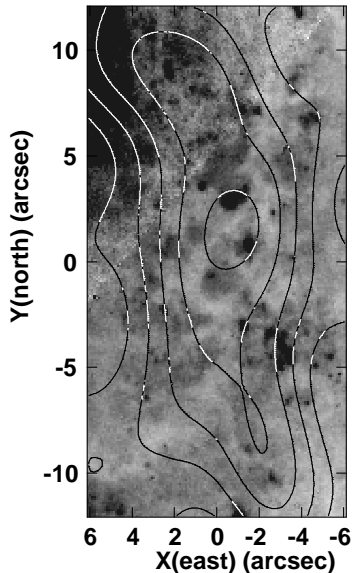
Figure 5. In greyscale the portion of the *HST* image containing the region of complex dust loops and centered on R.A., decl.(2000) = 10 10 09.006, −12 26 11.80. This is overlaid with contours at (3, 4, 5, 6, 7) × the rms noise from the $\lambda6$ cm radio continuum image with $7.4'' \times 5.5''$ (HPBW) resolution. The rms noise is 0.0224 mJy beam^{-1}, equivalent to $T_b = 0.029$ K. Some of the extended $\lambda6$ cm emission here may be from shocks associated with the dust loops and feathers.

is where the string of blue clumps intersects Sandage's peculiar arm. North of Feature f there is extended $\lambda6$ cm radio continuum emission along Sandage's peculiar arm. This is probably mainly synchrotron emission from shocked gas, since extended radio emission from arms in galaxies is usually nonthermal. We interpret this $\lambda6$ cm emission feature to mean that the portion of Sandage's arm from Feature f northwards is in the disk. The Hα emission, including the Feature f knot, is faint, perhaps due to extinction, but the 12 μm emission (see Figure 6) from this general area is relatively bright. The $\lambda6$ cm radio emission here contrasts with that from the *triangle*. Aside from an Hα and $\lambda6$ cm radio continuum star-forming clump between apices a and b on Sandage's peculiar arm, the *triangle*, including apices a and b, is not prominent in the $\lambda6$ cm radio continuum. Emission at $\lambda6$ cm from the region of complex dust loops partly overlaps apex c, but the latter does not appear as a distinct clump at $\lambda6$ cm. We conclude that *there are no shocks at the arm-crossing "X"'s of the triangle, and thus the arms that appear to cross at the apices of the triangle must be in different planes.*

Thus, whereas the part of Sandage's peculiar arm from Feature f northwards appears to be in the disk, the part of this arm that forms the eastern side of the *triangle* is not in the disk.

The distribution of the brighter $\lambda6$ cm emission in NGC 3145 has a somewhat ring-like appearance, composed of the brighter portions of the B-band spiral in the northern half of the galaxy, the section of Sandage's peculiar arm north of Feature f, and connections between these (see Figures 3 and 4). This contrasts with the distribution of 12 μm emission. In Figure 6, contours of the *WISE* 12 μm emission are overlaid on the $\lambda6$ cm radio image in greyscale. The locations of the nucleus,

apex a, and apex b are denoted by a plus sign, a five-pointed star, and a small triangle symbol, resp. The brightest 12 μm sources are at the locations of a) the northern $\lambda6$ cm clump on the spiral arm north of the nucleus, b) the region of complex dust loops, and c) the nucleus. Aside from these three sources, the brightest 12 μm emission is from the central hole in the distribution of $\lambda6$ cm emission. Similarly, with the *WISE* 22 μm image, whose resolution is a factor of 2 worse than the 12 μm image, the brightest emission is from the central hole in the $\lambda6$ cm distribution and from the northern $\lambda6$ cm clump on the spiral arm. Thus there is a lot of warm dust in the inner disk/bar/bulge of NGC 3145 but not a similar concentration of cosmic-ray electrons.

In Section 3.1 we noted that the arm outlining the western edge of the *triangle* decreases in prominence from B to V to R. Since this arm is not prominent in Hα either, it appears that optical emission from this arm may be dominated by A and/or B stars. This may help constrain the age of this feature.

Feature d in Figure 1 marks where the *branch* departs from the main spiral arm on the northeastern side of NGC 3145. Since there is no string of Hα knots along the *branch*, it does not meet the definition of a spur as given by La Vigne et al. (2006). A clump prominent in Hα and $\lambda6$ cm emission lies on the main spiral arm near this point. In Section 4.2.2, we shall see that there is a large difference in velocity between the spiral arm and the *branch* at feature d.

4. H I PROPERTIES OF NGC 3145

4.1. *H I Images*

Figure 7 displays the line-of-sight column density N(HI) image of the three galaxies in the system in greyscale and contours with $22''$ resolution. Table 4 lists the basic H I properties of the NGC 3145 triplet from our observations.

In the top panel of Figure 8 N(HI) contours are overlaid on the B image of NGC 3145 in greyscale. The distribution of H I emission from NGC 3145 is not axisymmetric; it consists of three major concentrations plus fainter extended emission and a trough $6''$ to $26''$ southeast of the nucleus. The brightest H I concentration is northeast of the nucleus and includes Feature d. This region has an H I mass M(HI) $= 1.8 \times 10^9$ $M_\odot$. It is elongated to the south, not along the main spiral arm but along the *branch* or a bit to the east of it. At $20''$ south of Feature d, the H I emission from the *branch* is still bright, whereas the H I emission from the spiral arm is near the trough. We conclude in Section 4.2.2 that this major H I concentration cannot be a single entity. The second brightest H I concentration is southwest of the nucleus and has M(HI) $= 1.4 \times 10^9$ $M_\odot$ if we omit its southern tail along the spiral arm. The third brightest H I concentration lies on the northwestern part of the two northern spiral arms, and its brightest part coincides with the most luminous $\lambda6$ cm clump in the galaxy. Its M(HI) $= 6 \times 10^8$ $M_\odot$. These H I masses are comparable to those of massive H I clouds in a number of interacting galaxy pairs - see Kaufman et al. (1999) and references therein. This suggests that the massive H I concentrations in NGC 3145 could have resulted from an encounter.
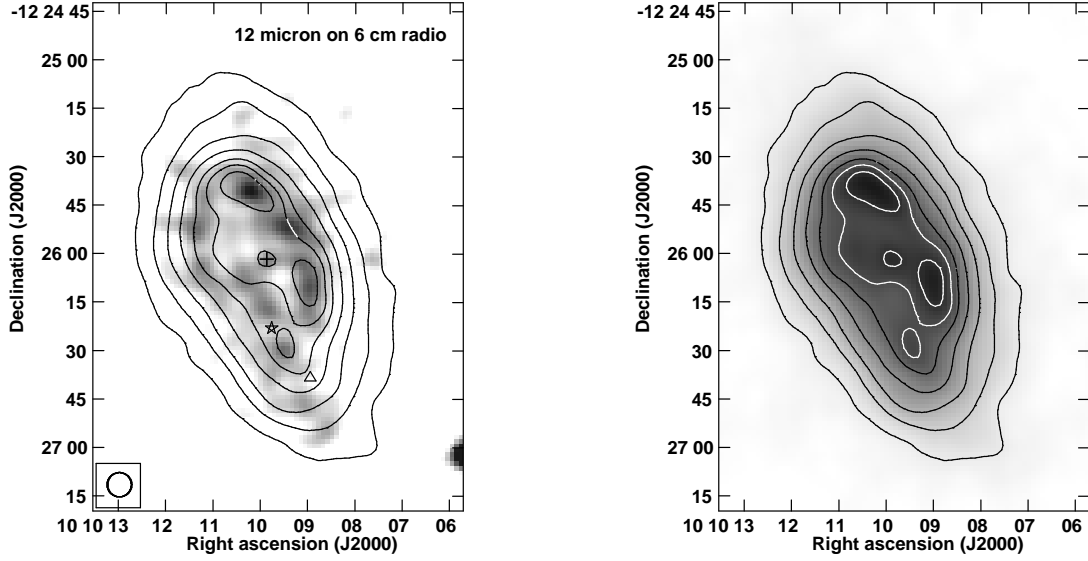
Figure 6. Left panel: Contours of *WISE* 12 μm emission overlaid on λ6 cm radio continuum in greyscale. The locations of the nucleus, apex *a*, and apex *b* of the *triangle* are denoted by a plus sign, a five-pointed star, and a small triangle symbol, resp. Right panel: Greyscale plus contour display of the *WISE* 12 μm image. Unlike the λ6 cm radio emission, the distribution of 12 μm emission is not somewhat ring-like.

Table 4
Basic H I Properties of the NGC 3145 Triplet

Characteristic	NGC 3145	NGC 3143	PGC 029578
Velocity Range of HI emission (km s^{-1})	3407 to 3919	3491 to 3581	3407 to 3623
Heliocentric $v_{\rm sys}$ (km s^{-1})	3655.9 $\pm$ 0.2	3530 $\pm$ 5	3512 $\pm$ 5
PA of receding major axis:			
Kinematic	205.44° $\pm$ 0.06°	$\cdots$	270° $\pm$ 3°
Isophotal	204° $\pm$ 2°	235° $\pm$ 5°	283° $\pm$ 5°
PA of kinematic minor axis	−60° $\pm$ 2°	$\sim$ 0°	173° $\pm$ 3°
Kinematic i	50.3° $\pm$ 0.3°	$\cdots$	$\cdots$
Isophotal i	55° $\pm$ 1°	$\leq$ 35°	61° $\pm$ 2°
HI diameter	262″ $\pm$ 2″	52″ $\pm$ 2″	122″ $\pm$ 2″
HI diameter/D_{25}	1.35 $\pm$ 0.09	1.00 $\pm$ 0.17	1.20 $\pm$ 0.20
Integrated HI flux S(HI) (Jy km s^{-1})	20.4	0.91	4.72
M(HI) ($M_\odot$)	1.44 $\times$ 10^{10}	6.5 $\times$ 10^8	3.33 $\times$ 10^9
Dynamical mass $M_{\rm dyn}$ ($M_\odot$)[a]	5.0 $\times$ 10^{11}	$\cdots$	2.2 $\times$ 10^{10}
M(HI)/$M_{\rm dyn}$[a]	0.029	$\cdots$	0.13
Maximum HI column density (atoms cm^{-2})	2.3 $\times$ 10^{21}	7.0 $\times$ 10^{20}	1.8 $\times$ 10^{21}

[a] out to $R = 127″ = 33$ kpc for NGC 3145, and $R = 50″ = 13$ kpc for PGC 029578

The total M(HI) of NGC 3145 is 1.4×10^{10} $M_\odot$. Its ratio of M(HI)/$L_{\rm B} = 0.17$ $M_\odot L_\odot^{-1}$, which is close to the median value for galaxies of the same Hubble type (Sbc) in Roberts & Hayes (1994).

The NGC 3145 first moment image (often called the velocity field) is displayed as contours overlaid on the *MDM B* image in greyscale in the bottom panel of Figure 8. The velocity dispersion image, uncorrected for the velocity gradient across the synthesized beam, is displayed in greyscale with velocity-field contours overlaid in the left panel of Figure 9, and the velocity dispersion image after correction for the velocity gradient is displayed in greyscale with N(HI) contours overlaid in the right panel of Figure 9. The first moment and velocity dispersion images are from the cube with lowest rms noise (Cube 1) and are blanked where N(HI) $\leq 1.9 \times 10^{20}$ atoms cm^{-2}. A plus symbol marks the location of the nucleus. In the velocity-dispersion figures (and in other figures below),

the locations of apex *a* and apex *b* of the *triangle* are denoted by the five-pointed star and the small triangle symbol, resp.

The velocity field exhibits some mild irregularities but not the highly distorted velocity fields found in some interacting galaxies, e.g. NGC 2207 (Elmegreen et al. 1995) or NGC 2535 (Kaufman et al. 1997). Along the *branch* there are kinks (or wiggles) in the velocity contours. At the arms where the λ6 cm radio emission is prominent in Figure 3, there is no evidence from Figure 8, or from one made from the C-array data with 10 km s^{-1} velocity resolution, of kinks (or wiggles) in the isovelocity contours due to streaming motions. If the radial component of streaming motions dominates, such kinks should be **u**-shaped on the western side and **n**-shaped on the eastern side of the galaxy. Either the somewhat ring-like distribution of λ6 cm emission is not expanding or our H I observations have too low a spatial resolution to re-
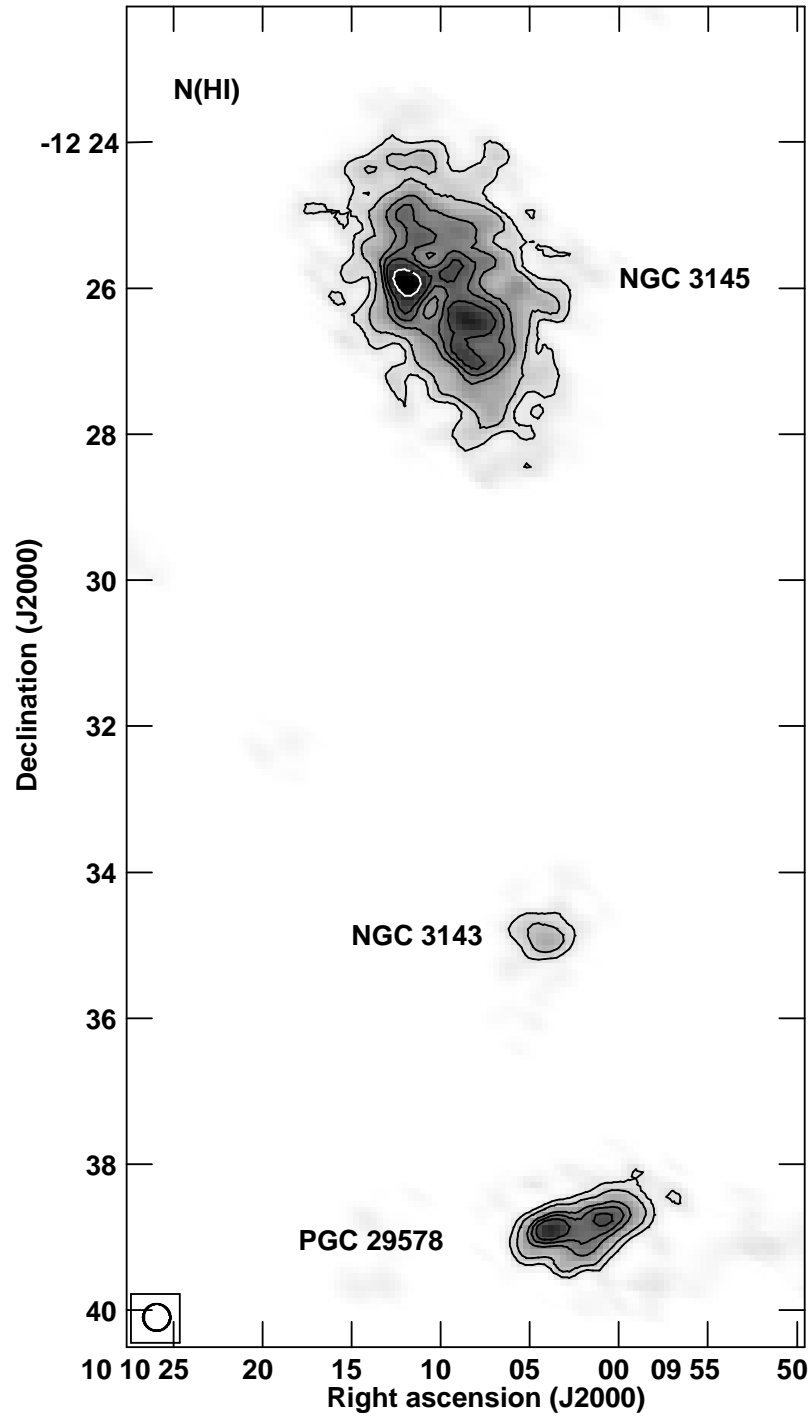
Figure 7. Greyscale plus contour display of the N(HI) image of the NGC 3145 triplet with resolution $= 22''$. Contour levels are at 100, 200, 400, 500, 600, and 800 Jy beam^{-1} m s^{-1}, where 100 Jy beam^{-1} m s^{-1} corresponds to a line-of-sight column density N(HI) $= 2.3 \times 10^{20}$ atoms cm^{-2}. The H I distribution in NGC 3145 is not axisymmetric; there is a trough at $6''$ to $26''$ southeast of the nucleus and three major H I concentrations (NE, SW, and NW of the nucleus.)
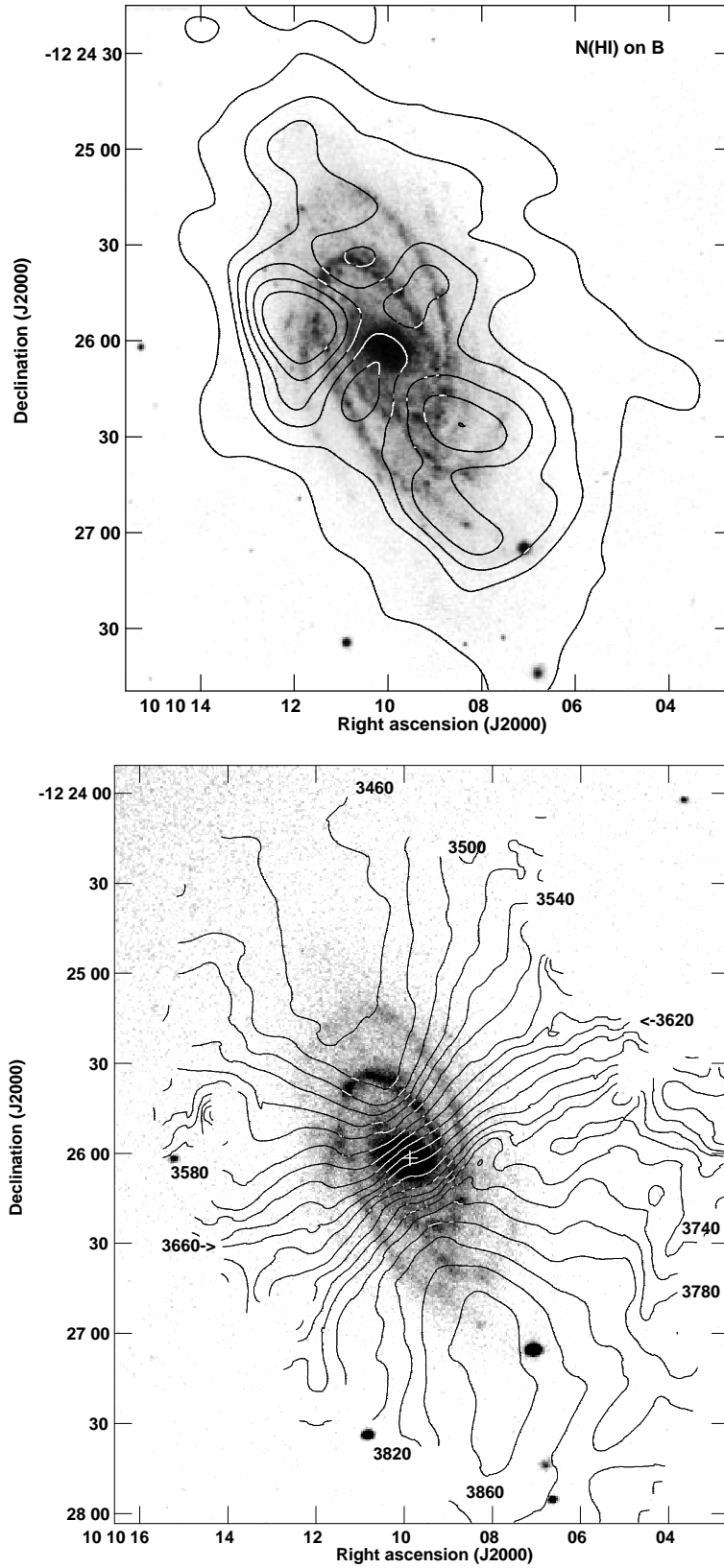
Figure 8. Top: B image of NGC 3145 in greyscale overlaid with $N(\mathrm{HI})$ contours. Contour levels are at 200, 400, 500, 600, 700, 800 $\mathrm{Jy\,beam^{-1}\,m\,s^{-1}}$, where 100 $\mathrm{Jy\,beam^{-1}\,m\,s^{-1}}$ corresponds to $N(\mathrm{HI}) = 2.3 \times 10^{20}$ atoms cm^{-2}. The major H I concentration northeast of the nucleus is elongated to the south, not along the main spiral arm but along the *branch* or a bit to the east of it. Bottom: Contours of the first moment image of NGC 3145 overlaid on the *MDM B* image in greyscale, with a plus symbol at the nucleus. The contour interval is 20 km s^{-1}. Along the *branch* there are kinks in the isovelocity contours.
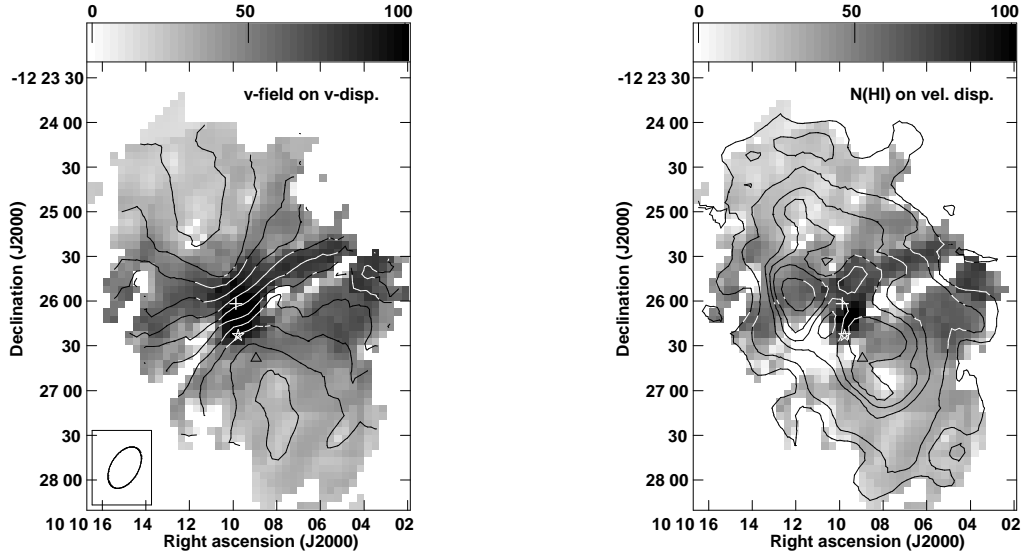
Figure 9. Left: Velocity field contours overlaid on a greyscale display of the velocity dispersion image before correction for the velocity gradient across the beam. Right: N(HI) contours of NGC 3145 from Figure 7 overlaid on greyscale display of the velocity dispersion image corrected for the velocity gradient. In both panels the units on the greyscale wedge are km s^{-1}, and the locations of the nucleus, apex a and apex b of the *triangle* are marked by the plus symbol, the five-pointed star, and the small triangle symbol, resp. Blanked pixels are white.

veal an expansion. A resonance ring produced by a bar would not be expanding.

The velocity dispersion image that is corrected for the velocity gradient across the synthesized beam has particularly high values for the velocity dispersion σ_v at apex a of the *triangle* and in the region of the complex dust loops. For the oddities labelled in Figure 1, Section 4.2.2 compares numerical values of σ_v before and after this correction. High values for the corrected σ_v may result, in part, because the line-of-sight intercepts gas at various altitudes above the disk and at various radial distances, in addition to streaming motions on small spatial scales and turbulence within the disk.

4.2. *Analysis of H I Motions*

4.2.1. *Large Scale Anomalies*

We use the AIPS program GAL to fit a model rotation curve to the first moment image of NGC 3145 and determine its kinematic parameters. The routine assumes a flat disk in rotation. The residuals from such a fit may reveal whether significant parts of the the galaxy are not in a flat disk or have motions other than rotation. We first used GAL to fit a Brandt model (Brandt 1960) rotation curve to our first moment image of the disk as a whole. It finds a kinematic center within 1″ of the optical nucleus, a systemic velocity $v_{\rm sys} = 3655.9 \pm 0.2$ km s^{-1}, close to the optical value of 3652 ± 6 km s^{-1}, and a position angle of the receding major axis PA $= 205.4° \pm 0.06°$, consistent with the isophotal value of 205° from *2MASS* $K_{\rm s}$ and from the N(HI) outer isophotes.

On the other hand, the velocity-residual field exhibits a curious asymmetry on and near the minor axis. In Figure 10 , the residual velocity image (observed minus model) is displayed in greyscale and contours, and the locations of the kinematic center, apex a, and apex b are denoted by the plus sign, the five-pointed star, and the small triangle symbols, resp. Lines are drawn in this figure to divide the galaxy into four quadrants: these

are centered on the receding major axis in the SSW, the near-side (relative to us) minor axis in the WNW, the approaching major axis in the NNE, and the far-side minor axis in the ESE. On the near-side minor axis, the residual velocities are receding from us, whereas on the far-side minor axis, the residual velocities are approaching us. The minor axis is where radial or z-motions (perpendicular to the disk) would be most apparent. The observed asymmetry would be consistent with radial inflow or with z-motions. The asymmetry region overlaps part of the ring-like distribution of λ6 cm emission, so if the motions producing the asymmetry were radial, this would argue against an expanding pseudo-ring because it would have to be a contracting pseudo-ring instead. We conclude below that the more likely explanation is z-motions. The residual velocities have somewhat greater magnitude on the WNW minor axis (25 to 62 km s^{-1}) than on the ESE minor axis (-19 to -27 km s^{-1}). At the location of the *triangle*, the residual velocities are small $\simeq 4$ km s^{-1}.

With the values of the kinematic center and systemic velocity fixed as above, we used GAL to fit separate Brandt rotation curves to the receding and approaching major-axis quadrants. The results are listed in Table 5 and displayed in Figure 11. Brandt curves are good fits to the major axis quadrants, and for values of the face-on radius $R \geq 30″$, they yield velocity differences of less than 5% between the approaching and the receding sides. The solution for the major axis quadrants gives a value for the inclination $i = 50.3° \pm 0.3°$, (a little smaller than the isophotal value $i = 55°$ from the *2-MASS* isophotes and the N(HI) outer isophotes) and a maximum velocity of the rotation curve $v_{\rm max} = 271 \pm 1$ km s^{-1}. This maximum occurs at $R_{\rm max} = 68.6″ = 18$ kpc on the receding side and $76.5″ = 20$ kpc on the approaching side.

To provide more information about noncircular motions, Figure 12 displays H I line profiles, spaced 15″ apart (i.e, every third spatial pixel) from Cube 1 for the entire northern half of NGC 3145. Figure 13 does the
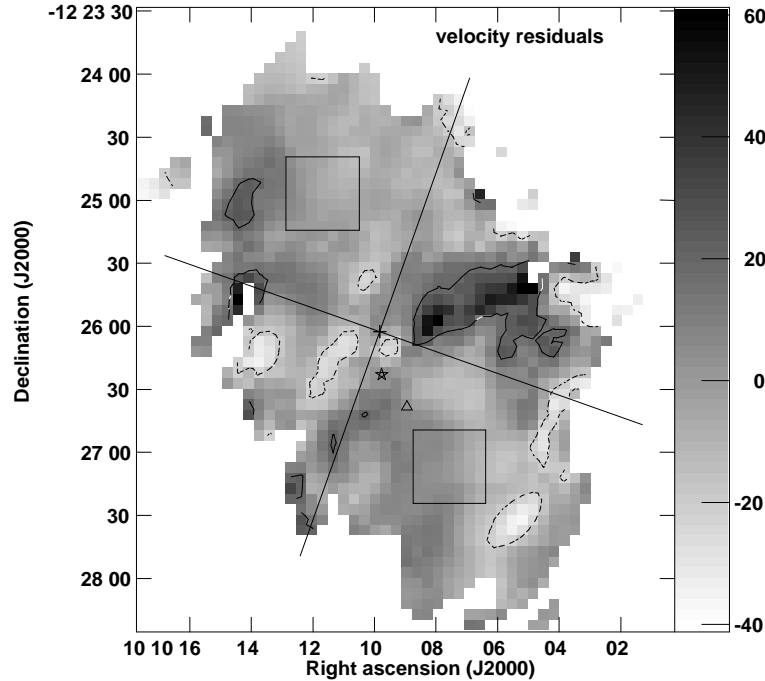
Figure 10. Greyscale and contour display of velocity residuals from fitting a Brandt model rotation curve to the first moment image of NGC 3145 as a whole. The contours are at 20 km s^{-1} and -20 km s^{-1}, and the units on the greyscale wedge are km s^{-1}. The locations of the nucleus, apex a and apex b are marked as in Figure 9. Lines are drawn to divide the galaxy into four quadrants: receding major axis (SSW), near-side minor axis (WNW), approaching major axis (NNE), and far-side minor axis (ESE). The boxes on the major axis are the R_{max} boxes where we fit the line-profile at each pixel with the sum of two Gaussians.

Table 5
Velocity Parameters from fitting the data with GAL

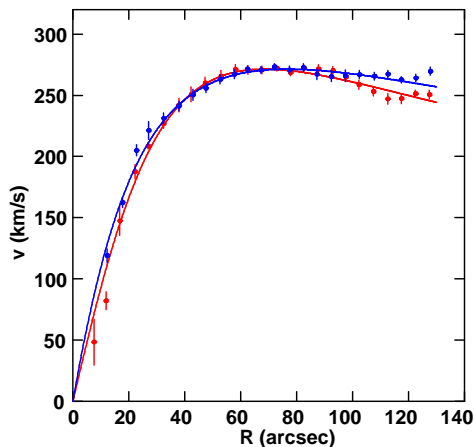| Quadrant	i (°)	v_{max} (km s^{-1})	R_{max} ($''$)	n_{B}
whole disk	46.1 ± 0.2	286.8 ± 0.9	74.6 ± 0.5	1.44 ± 0.02
NNE Major Axis	50.6 ± 0.3	271.4 ± 1.0	76.5 ± 0.9	1.28 ± 0.03
SSW Major Axis	50.1 ± 0.3	271.4 ± 1.1	68.6 ± 0.5	1.84 ± 0.03

Figure 11. Brandt rotation curve fits to major-axis quadrants of the first moment image of NGC 3145 with the receding major-axis quadrant in red and the approaching major-axis quadrant in blue.

same for the entire southern half of the galaxy. At distances $\gtrsim 35''$ from the nucleus, the line profiles on and near the approaching major axis (NNE side) consist of a large amplitude, narrow peak with an asymmetric, extended, high velocity wing, and the line profiles on and near the receding major axis (SSW) side consist of a large amplitude, narrow peak with an asymmetric, extended, low velocity wing. Since observed motions on a major axis cannot contain a contribution from radial inflow or radial outflow, the possible interpretations of the skewed wings in these profiles are out-of-plane gas in a thick disk with a slower rotation speed than the thin disk or z-motions of gas moving away from us (relative to the disk) on the approaching major axis and towards us (relative to the disk) on the receding major axis. As we find kinematic oddities on the minor axis as well as on the major axis, the simplest explanation for both is z-motions. Given the optical oddities that suggest out-of-plane arms in this galaxy, it is not surprising to find motions perpendicular to the disk. Taken together with the asymmetry in the residual velocities on and near the minor axis (see Figure 10), it seems that relative to the

disk, there is gas with z-motions away from us on and near the NNE major axis and near the WNW minor axis and z-motions towards us on and near the SSW major axis and near the ESE minor axis. This anti-symmetry of the z-motions suggests the disk is undergoing warping as a result of a close passage by a companion. We detect these warping motions out to a radius of at least $105''$.

For the line-profiles near the major axis that consist of just a major peak plus a skewed tail, we fit the sum of two Gaussians to each profile in the two boxes marked in Figure 10. These $35'' \times 35''$ boxes are centered approximately at $R_{\max}$ on the major axis, and we shall refer to them as the $R_{\max}$ boxes We assume that the large-amplitude peak in the profile is from gas in the disk and that the skewed tail is from gas moving perpendicular to the disk. The goals are to determine some information about the H I gas involved in the z-motions and to determine how much the rotation curve derived from the H I velocity field at these positions is affected by the z-motions. Let the subscript 1 refer to the parameters from the Gaussian fit at the large-amplitude peak in each line profile and subscript 2 refer to the parameters from the Gaussian fit to the skewed tail. Table 6 lists the mean values from the two-Gaussian fits to the following parameters for the $R_{\max}$ boxes: (a) the difference $v_1 - v_2$ in the line-of-sight central velocities of the Gaussians, (b) the difference $v - v_1$ between the velocity v of the velocity field in the first moment image and the central velocity v_1 of the large-amplitude peak, (c) the FWHM widths of the Gaussians, and (d) the ratio $N(\mathrm{HI})_2/N(\mathrm{HI})_1$ of the column densities. Locations with bad solutions or large uncertainties are omitted. The uncertainty attached to each mean is the mean of the Gaussian uncertainties. Also listed are the values of the standard deviation s of the sample.

On the receding major-axis, the mean value of $v - v_1$ for the $R_{\max}$ box is -15 ± 1 km s^{-1} with $s = 4$ km s^{-1}, and for positions closest to the major axis the mean is -11 km s^{-1} with $s = 2$ km s^{-1}. On the approaching major axis, the mean value of $v - v_1$ for the $R_{\max}$ box is 12 ± 1 km s^{-1} with $s = 6$ km s^{-1}, and for positions closest to the major axis the mean is 8 km s^{-1} with $s = 3$ km s^{-1}. Therefore the correction for this effect on $v_{\max}\sin i$ amounts to only about 5%, which is negligible.

For a spherically symmetric mass distribution, the dynamical mass $M_{\mathrm{dyn}}(R)$ within face-on radius R is $M_{\mathrm{dyn}}(R) = R(v_{\mathrm{rot}})^2/G = 2.33 \times 10^5 R(v_{\mathrm{rot}})^2$ $M_\odot$ for R in kpc and circular velocity v_{rot} in km s^{-1}. We fit the velocity data in the major axis quadrants out to $R = 127'' = 33.3$ kpc, which is (approximately) the extent of significant major-axis emission in the $N(\mathrm{HI})$ image. At this radius, the fitted curves in Figure 11 have an average $v_{\mathrm{rot}} = 252 \pm 6$ km s^{-1}, which gives a dynamical mass $M_{\mathrm{dyn}} = 5.0 \times 10^{11}$ $M_\odot$. Since $M(\mathrm{HI}) = 1.4 \times 10^{10}$ $M_\odot$, H I accounts for only 3% of the dynamical mass out to this radius. The radius of $127''$ that we use for M_{dyn} is greater than the Holmberg radius of $103''$ used by Faber & Gallagher (1979) for M_{dyn}. At R $= 103''$ our data have an average v_{rot} of 263 ± 3 km s^{-1}, which is only 5% greater than the value of 250 km s^{-1} used by Faber & Gallagher (1979). Thus aside from the difference in the adopted distance of NGC 3145, our value for M_{dyn} out to the Holmberg radius is consistent with

theirs.

The magnitude of the difference $|v_1 - v_2|$ in the line-of-sight central velocities in the $R_{\max}$ box on the receding side 47 ± 7 km s^{-1} is marginally consistent, within the uncertainties, with its magnitude 37 ± 3 km s^{-1} in the $R_{\max}$ box on the approaching side. This is compatible with the suggestion that the skewed tail in these line profiles was produced by the same mechanism on both sides of the galaxy.

On both sides, the FWHM width of the Gaussian fit to the line profile is about 20 km s^{-1} broader for the skewed tail than for large amplitude peak. The larger velocity width for the skewed tail could result from a velocity gradient along the flow .

For the ratio $N(\mathrm{HI})_2/N(\mathrm{HI})_1$ of the column densities from the Gaussian fits, we restrict to positions where the propagated uncertainty in this ratio is less than 50%; this eliminates about half of the positions in the above boxes. Then for the $R_{\max}$ box on the receding side, the mean value of $N(\mathrm{HI})_2/N(\mathrm{HI})_1 = 0.4 \pm 0.1$ with standard deviation s of the sample $= 0.2$ and range $= 0.2$ to 0.9. For the $R_{\max}$ box on the approaching side, the mean value of this ratio $= 0.9 \pm 0.2$ with $s = 1.0$ and range $= 0.20$ to 3.5. We conclude that the amount of gas involved in the z-motions is not insignificant but varies considerably with position.

Another way of analyzing the velocities in NGC 3145 is to look at the image of the skewness of the line-profiles in Figure 14. The parameter displayed is the dimensionless Fisher-Pearson coefficient of skewness

$$g_1 = \frac{m_3}{(\sigma_{\mathrm{v}})^3}$$

where m_3 is the third moment of the velocity data. For a sample of size n, g_1 needs to be multiplied by a correction factor

$$\frac{[n(n-1)]^{1/2}}{n-2}.$$

For Cube 1, this correction factor varies from 1.06 near the center to 1.2 in the outskirts of NGC 3145. In Figure 14, regions in green have negligible skewness of the line-profiles, i.e., $|g_1| < 0.5$, and the rest of the galaxy has moderate to high skewness of the line-profiles. This image demonstrates that (1) most of the half of the galaxy from position angle PA $= 60°$ to PA $= 240°$ has negative skewness of the line-profiles, i.e., gas moving towards us relative to the disk. (2) In the other half of the galaxy there are large areas of positive skewness, i.e., gas moving away from us relative to the disk.

4.2.2. Small Scale Anomalies

We study the various oddities marked in Figure 1 by inspecting their H I line-profiles. For NGC 3145, we find the line-profiles to be more revealing than position-velocity diagrams are.

For features of interest, Table 7 lists values of σ_{v} of the H I gas before and after correction for the mean velocity gradient across the PSF. These are from Cube 1, the cube with 21 km s^{-1} velocity resolution. The correction for these features decreases the velocity dispersion by 15% to 32%. For comparison, this Table also contains the values of σ_{v} at the diametrically-opposite locations of some of the features. These are listed as "opp. apex
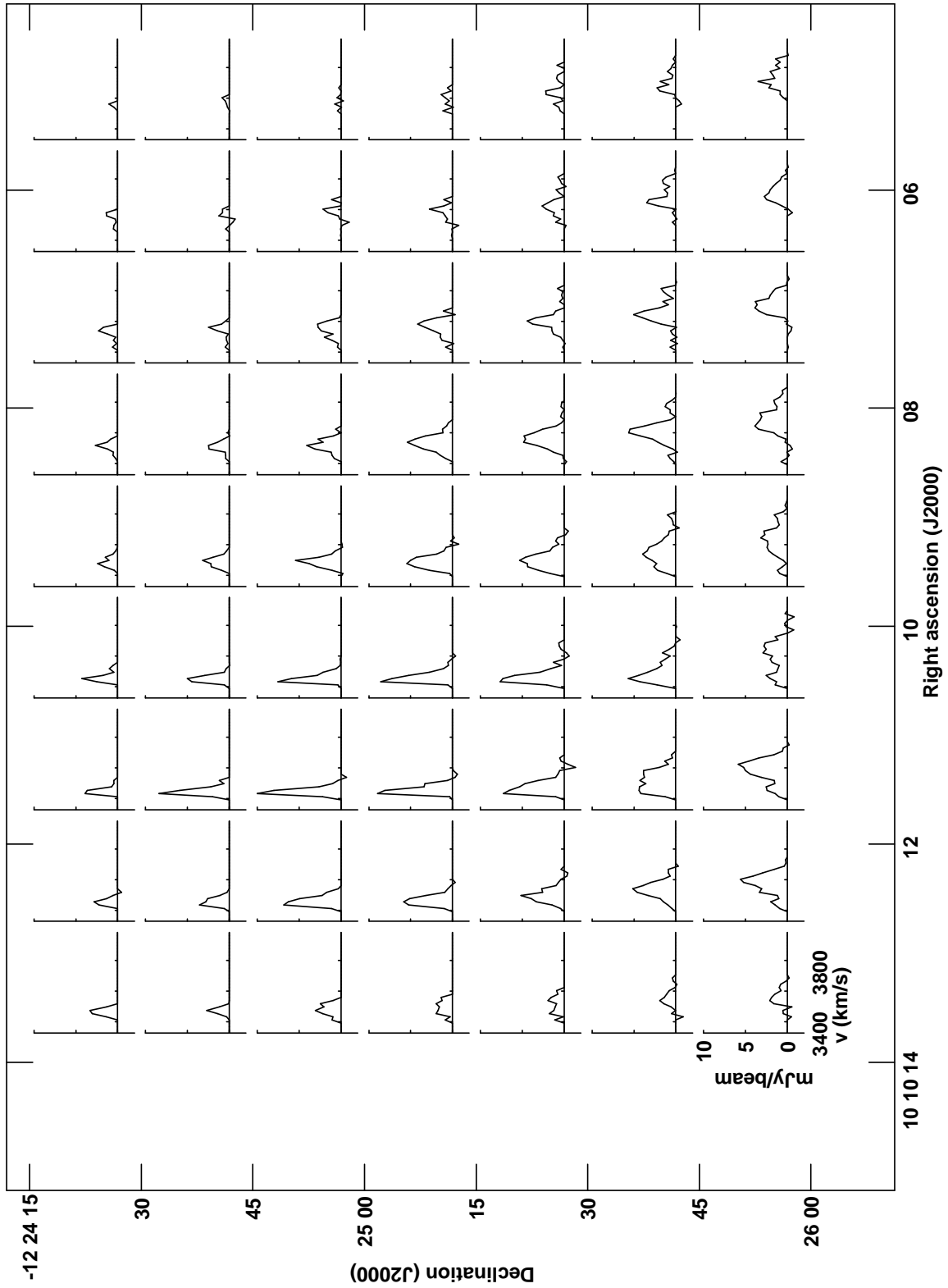
Figure 12. H I line-profiles spaced $15''$ apart from Cube 1 (with $\sigma_{\mathrm{rms}} = 0.50$ mJy beam^{-1} and 21.2 km s^{-1} resolution) for the entire northern half of NGC 3145. The line-profiles on and near the major axis consist of a large amplitude peak with a skewed wing towards higher velocities.
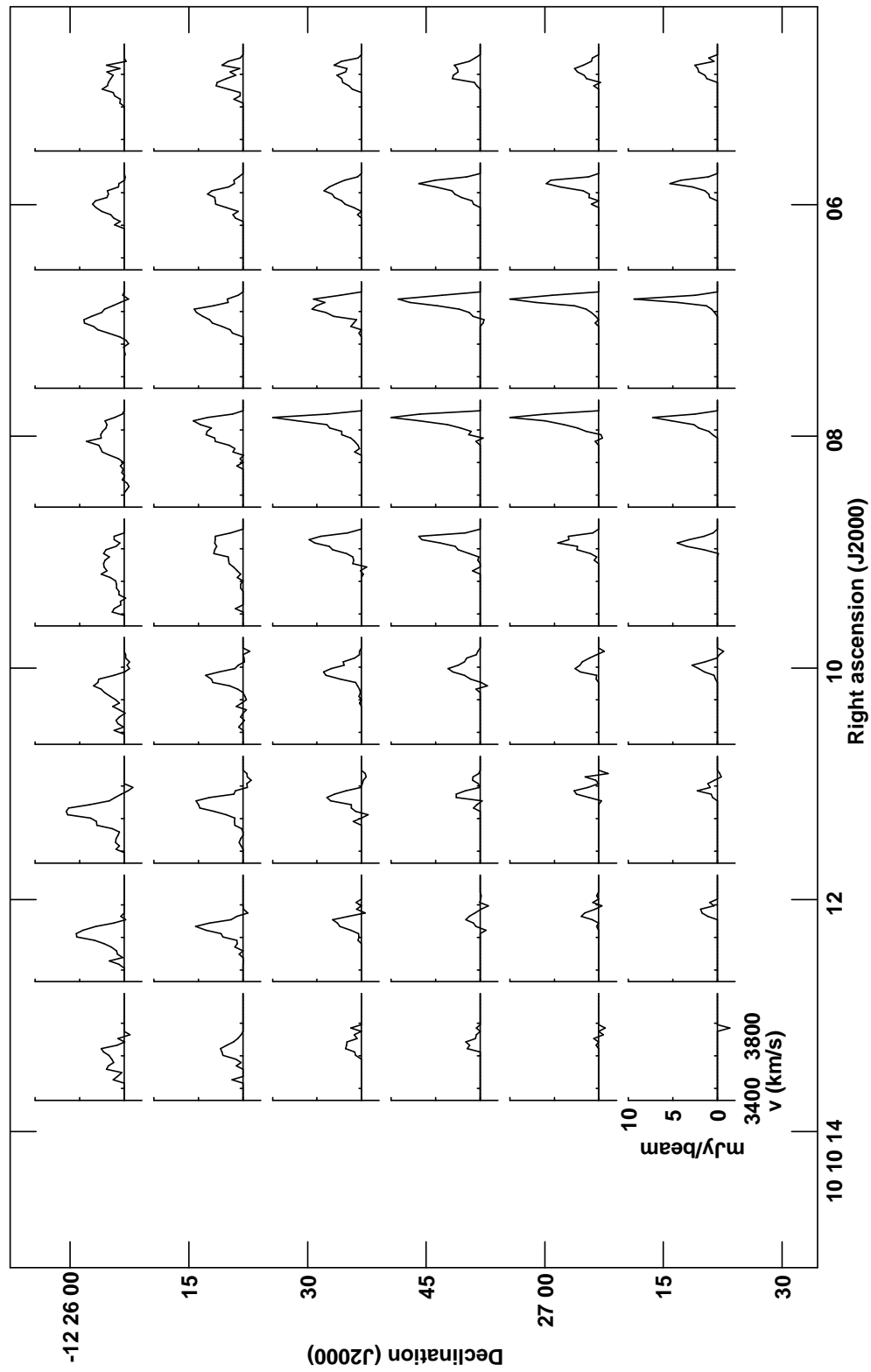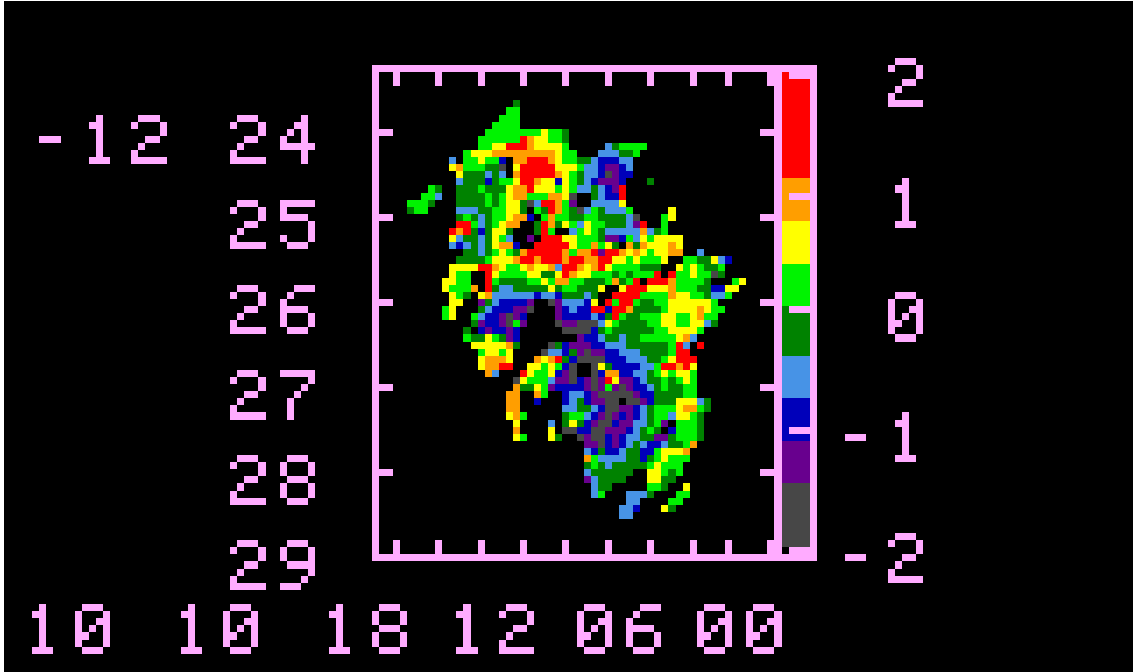
Figure 13. H I line-profiles spaced $15''$ apart from Cube 1 for the entire southern half of NGC 3145. The rms noise = 0.50 mJy beam^{-1}. The line-profiles on and near the major axis consist of a large amplitude peak with a skewed wing towards lower velocities.

Figure 14. Display of the Fisher-Pearson coefficient of skewness of the line-profiles in NGC 3145. Regions in green have negligible skewness of the line-profiles. The rest have moderate to high skewness. *Most of the half of the galaxy from PA = 60° to PA = 240° has negative skewness of the line profiles, i.e., gas moving towards us relative to the disk. The other half of the galaxy has large areas with positive skewness, i.e., gas moving away from us relative to the disk.*

Table 6
Two-Gaussian Fits to Line-Profiles in R_{max} Boxes

Parameter	Receding Side mean	s^{a}	Approaching Side mean	s
$v - v_1$ (km s^{-1})	-15 ± 1	± 4	12 ± 1	± 6
$v_1 - v_2$ (km s^{-1})	47 ± 7	± 11	-37 ± 3	± 7
$(FWHM)_1$ (km s^{-1})	41 ± 5	± 6	31 ± 4	± 3
$(FWHM)_2$ (km s^{-1})	67 ± 12	± 10	50 ± 9	± 10
$N(\mathrm{HI})_2/N(\mathrm{HI})_1$	0.4 ± 0.1	± 0.2	0.9 ± 0.2	± 1.0

^{a} s is the standard deviation of the sample

a," "opp. apex b," etc. Since the line-profiles are not corrected for the velocity gradient, one does well to keep in mind the size of the correction to σ_v when viewing the line-profiles since a large velocity gradient plus finite spatial resolution artificially broaden a line-profile. Our method of correcting the velocity dispersion is less accurate in regions, such as near the galaxy center, where the velocity gradient changes significantly across the PSF. This inaccuracy contributes to the very high values of the corrected σ_v in part of the region of complex dust loops and at Feature f (see velocity contours in Figure 8).

All of the corrected values of σ_v for the features in Table 7 (36 km s^{-1} to 68 km s^{-1}, if we exclude Feature f and the region of complex dust loops) are large compared to the values of 6 - 13 km s^{-1} found by Kamphuis (1993) for the H I gas in undisturbed spirals, but are comparable to the high values of σ_v measured in some galaxy pairs undergoing close encounters (Elmegreen et al. 1995; Kaufman et al. 1997, 1999).

The clearest situation is Feature d in Figure 1 . Fig-

ure 15 displays H I line-profiles, spaced $5''$ apart, for Feature d and its surroundings. The panel labelled "d" is where the branch and the main spiral arm appear to intersect, and the panel just below it is where the *branch* departs from the spiral arm. The four panels in the upper right corner of Figure 15 (i.e., the intersection of rows 4 and 5, with columns 4 and 5, where we number rows and columns from the bottom left corner of the figure) are located along the main spiral arm. The greatest amplitude peak in their line-profiles is at 3454 km s^{-1}. The six panels in the bottom left corner of the figure (the intersection of rows 1, 2, and 3 with columns 1 and 2) are located along the *branch*. The greatest amplitude peak in their line-profiles is at ~ 3620 km s^{-1}. The line-profiles at the panel where the *branch* and the main arm appear to intersect and at the panel where the *branch* departs from the main arm have two main peaks: one at 3623 km s^{-1} (i.e., the *branch*) and the other at 3475 km s^{-1}(i.e., the main spiral arm). Although optically feature d looks like a branch of the spiral arm, the ~ 150 km s^{-1} differ-
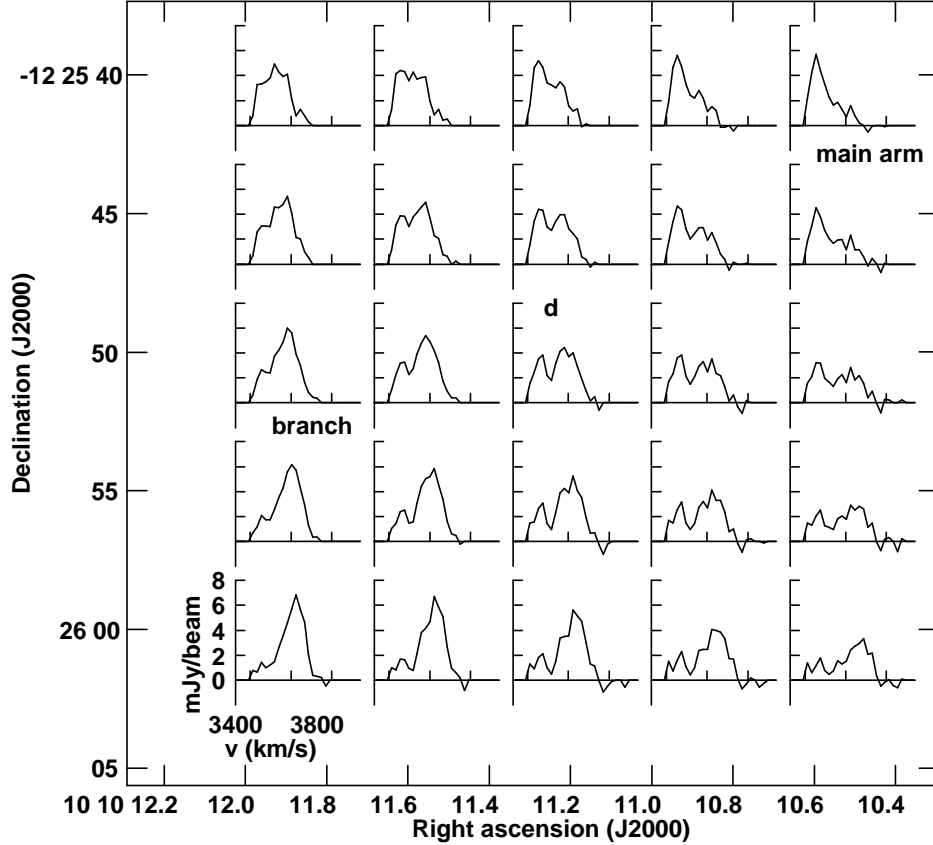
Figure 15. H I line-profiles of the main spiral arm and the *branch* on the northeastern side of NGC 3145 from Cube 1, spaced 5″ apart. The rms noise is 0.5 mJy beam^{-1}. The panel labelled "d" is where the *branch* appears to intersect the main spiral arm. The *branch* is the peak at 3623 km s^{-1}, and the main spiral arm is the peak at 3475 km s^{-1} in the line-profile. The ~ 150 km s^{-1} difference in velocity between the *branch* and the main spiral arm where in projection they appear to intersect implies that *the branch is a tidal arm moving away from us.*

Table 7
Corrected Velocity Dispersions

Location	σ_{v} (km s^{-1})	Corrected σ_{v} (km s^{-1})
apex *a*	94	68
opp. apex *a*	60	40
apex *b*	50	36
opp. apex *b*	41	38
apex *c*	50	36
opp. apex *c*	57	50
triangle (mean)	72	49
opp. *triangle* (mean)	50	37
Feature *f*	111	83
opp. Feature *f*	98	85
complex dust-loops (mean)	93	79
Feature *d* (mean)	71	59
western antenna (mean)	54	46

ence in line-of-sight velocity between the *branch* and the main spiral arm where in projection they appear to intersect suggests that the *branch* is an out-of-plane feature moving away from us relative to the disk, and there may be large streaming motions along it. Thus *the branch is*

a tidal arm. To produce the observed structure, the perturbation needed an azimuthal component to draw out the tidal arm and a perpendicular component to make it extra-planar. The apparently major H I concentration at this location cannot be a single entity; instead one part is associated with the main spiral arm and another part with the *branch.* As noted in Section 4.1 (see Figure 8), the brighter H I here is elongated to the south, not along the main spiral arm but along the *branch* or a bit east of it, and the velocity field contours have wiggles along the *branch.*

Struck-Marcell (1990) comments that the optical *triangle* on the southern side of NGC 3145 looks like a swallowtail caustic. A swallowtail caustic is composed of five "intersecting" star streams. In his study of two-dimensional caustics with collisionless particles, he finds that such features may result from a slightly off-center direct collision with a smaller galaxy.

Our H I data do not have sufficient resolution to see individual gas streams in the *triangle*, and we note that once gas is included, a three-dimensional model would be needed. Instead, as a test we compare the H I line-profiles in the *triangle* with those in the diametrically-opposite region on the northern side of NGC 3145. Also for the features of interest, we compare the values of the corrected velocity dispersion in Table 7 with those at the diametrically-opposite locations. In Figure 16, the bot-
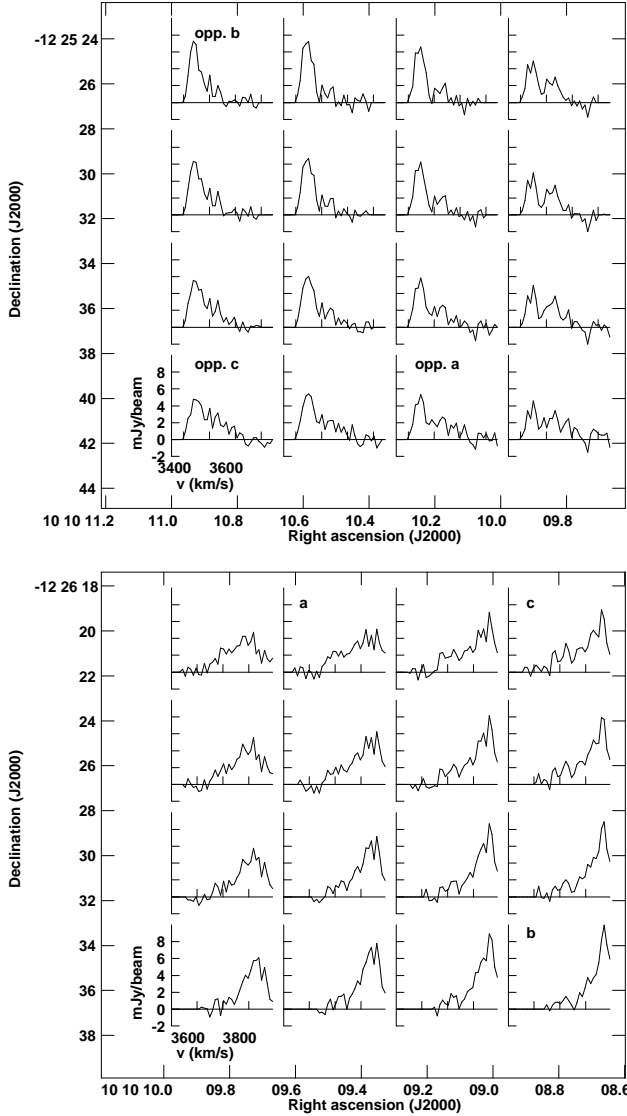
Figure 16. Bottom: H I line-profiles from the cube with 10.6 km s^{-1} resolution, spaced 5″ apart, for the *triangle*. The rms noise is 0.74 mJy beam^{-1}. The panels at apices a, b, and c of the *triangle* are labelled "a," "b," and "c," resp. Top: H I line-profiles for the diametrically-opposite region. The line-profiles labelled "opp. a", "opp. b", and "opp. c" are diametrically-opposite apices a, b, and c, resp. Only apex a differs significantly in shape and width of the line-profile from that of its diametrically-opposite counterpart.

tom panel displays H I line-profiles, spaced 5″ apart, for the *triangle* from Cube 3, which has a velocity resolution of 10.6 km s^{-1} and a spatial resolution of 27.3″ × 16.6″ (HPBW), BPA = −29°. The top panel displays the diametrically-opposite region, with line-profiles labelled "opp. a," "opp b," and "opp. c." Only apex a shows a significant difference when comparing its line-profile and corrected $\sigma_{\rm v}$ with those of the diametrically-opposite location. Apex a is where the inner spiral arm and Sandage's peculiar arm intersect in projection. Thus, our data cannot confirm the swallowtail interpretation of the apparent *triangle*.

If a slightly off-center direct collision were responsible for the anomalous features in NGC 3145, then to produce the observed warping motions over large spatial scales found in Section 4.2.1, the orbital tilt angle would
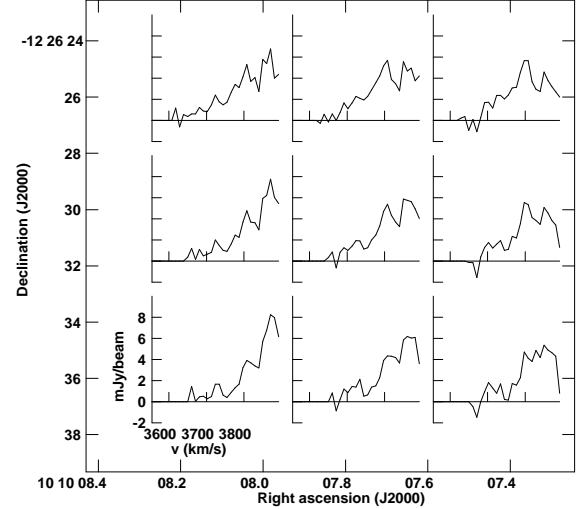

Figure 17. H I line profiles of the western-antenna continuation of Sandage's peculiar arm. These are from the cube with 10.6 km s^{-1} resolution, spaced 5″ apart. The rms noise is 0.74 mJy beam^{-1}. All but one of these line-profiles have two clearly distinct peaks separated by 56 ± 8 km s^{-1}. We attribute one of these peaks to Sandage's peculiar arm and the other to the disk.

have to be significantly less than 90° relative to the disk of NGC 3145. Our failure to find a strong expanding ring is consistent with an encounter that is not close to perpendicular.

The line-profile at apex b (see Figure 16) consists of a large amplitude, narrow peak plus an asymmetric, extended wing to lower velocities. Fitting the sum of two Gaussians to the line-profile at apex b in Cube 1 gives (a) for the large amplitude peak, a central velocity $v_1 = 3872 \pm 1$ km s^{-1} and $(FWHM)_1 = 42 \pm 3$ km s^{-1}, and (b) for the skewed wing, a central velocity $v_2 = 3818 \pm 11$ km s^{-1} and $(FWHM)_2 = 100 \pm 17$ km s^{-1}. Thus $v_1 - v_2 = 54 \pm 11$ km s^{-1}. These values for the line-of-sight velocity difference $v_1 - v_2$ and $(FWHM)_1$ are similar to the mean values listed in Table 6 for the warping motions in the receding-side $R_{\max}$ box (which is southwest of apex b and the western antenna). The value of $(FWHM)_2$ for apex b is somewhat greater than the mean for this $R_{\max}$ box. Unlike apex b, the $R_{\max}$ box does not contain an "X"-feature (where two arms appear to cross in projection). We note that two arms having the same line-of-sight velocity where they produce an "X"-feature could, nevertheless, be in different planes.

The western antenna is a continuation of Sandage's peculiar arm. Figure 17 displays western antenna line-profiles of feature e in Figure 1. These are for the smaller of the two boxes drawn on the *HST* image in that Figure. The line-profiles are from Cube 3 (the cube with 10.6 km s^{-1} resolution), spaced 5″ apart and do not resemble those at the diametrically-opposite location. Eight of the nine line-profiles in this figure exhibit two main, clearly distinct peaks of comparable amplitude. The mean separation in velocity between the two peaks is 56 km s^{-1} with a standard deviation s of the sample = 8 km s^{-1}. This is essentially the same as the value of $v_1 - v_2 = 54 \pm 11$ km s^{-1} at apex b. We attribute one of these peaks to Sandage's peculiar arm and the other to the disk. Like the *branch* on the northeastern side of NGC 3145, Sandage's peculiar arm appears to be a tidal arm,

but differs by only 56 km s^{-1} in line-of-sight velocity from that of the disk, whereas the *branch* differs by ~ 150 km s^{-1} from that of the disk.

In Section 3.2, we found that the portion of Sandage's peculiar arm from Feature f northwards appears to be in the disk but once this arm reaches the eastern side of the *triangle*, it is no longer in the disk. If Sandage's peculiar arm is a tidal arm coming from the central part of the galaxy, it is not surprising to find a shock front along its initial part until it emerges from the disk.

In summary, we find two types of extra-planar motions in NGC 3145: (i) an anti-symmetric, global warping of the disk and (ii) extra-planar tidal arms. Feature d is quite distinct from the warping motions on the northern side of the galaxy in terms of the size of the line-of-sight velocity difference between components of the line-profile (150 km s^{-1} versus 37 km s^{-1}) and the shape of the line-profile. In contrast to this, the line-of-sight velocity difference between Sandage's peculiar arm and the disk is similar in size to that of the warping motions. For these two extra-planar arms, the observed difference in line-of-sight velocity between the arm and the disk could be a combination of z-motions and streaming along the arm. We do not have sufficient information to determine the relative contributions of these two types of motions.

5. H I PROPERTIES OF NGC 3143 AND PGC 029578

Basic H I properties of the two companions, NGC 3143 and PGC 029578, are listed in Table 4. Both companions are on the receding side of NGC 3145 (see Figure 8) and have values of $v_{\rm sys}$ less than that of NGC 3145. There are no other galaxies near NGC 3145 that have published optical redshifts close to that of NGC 3145 or have H I detections.

The SB(s)b galaxy NGC 3143 at 8.97′ (= 141 kpc) south of NGC 3145 is the nearer to it of the two companions and has the smaller diameter. It is bluer in $B - V$ than NGC 3145 (see Table 1), and optically its spiral arms are brighter than the spiral arms of NGC 3145. In the top panel of Figure 18, N(HI) contours of NGC 3143 are overlaid on the B image from the Burrell-Schmidt telescope. The H I column densities in NGC 3143 are significantly lower than in NGC 3145 or in PGC 029578 (see Table 4 and Figure 7).

In K_s-band, the luminosity of NGC 3143 is 0.073 times the luminosity of NGC 3145. We adopt this as the stellar mass ratio of NGC 3143 to NGC 3145. If we assume that the total mass ratio of NGC 3143 to NGC 3145 is the same as the stellar mass ratio, then since the dynamical mass of NGC 3145 is $M_{\rm dyn} = 5.0 \times 10^{11}$ $M_\odot$ out to $1.3\times$ the optical radius, the estimated mass of NGC 3143 is $\sim 3.7 \times 10^{10}$ $M_\odot$.

The following comparisons indicate that NGC 3143 is somewhat deficient in H I. The H I mass M(HI) of NGC 3143 is 6.5×10^8 $M_\odot$, which is only 4.5% of the H I mass of NGC 3145. Thus the ratio of M(HI) to stellar mass is a factor of 1.6 greater in NGC 3145 than in NGC 3143. In NGC 3143, the ratio M(HI)$/L_{\rm B} = 0.085$ $M_\odot L_\odot^{-1}$. This value lies in the bottom 25% of Sab, Sb spirals in Roberts & Hayes (1994) and is half of its value in NGC 3145. This low value of M(HI)$/L_{\rm B}$ could be the result of more active star formation in NGC 3143 as indicated by its bluer $B - V$ color or of loss of some H I

by NGC 3143 in an encounter. The amount of molecular gas in these galaxies has not been measured.

We estimate the star formation rate (SFR) of NGC 3143 from the magnitudes listed by *WISE*. At 22 μm NGC 3143 has a magnitude $m(22\ \mu{\rm m}) = 6.173 \pm 0.055$ mag. Since it is 4 mag brighter at 12 μm than at 4.6 μm, NGC 3143 is a red source in the mid-infrared. To convert $m(22\ \mu{\rm m})$ to flux density $S_\nu(22\ \mu{\rm m})$, we use the zero-magnitude flux-density, the correction for red sources, and other information from the online *WISE* All-Sky Release Explanatory Supplement. This gives $S_\nu(22\ \mu{\rm m}){=}$ 26 mJy for NGC 3143. We extrapolate to 24 μm by taking $S_\nu \propto \nu^{-2}$. Then with a distance D of 54.8 Mpc and $L(24\ \mu{\rm m}) = \nu L_\nu$, the luminosity $L(24\ \mu{\rm m})$ of NGC 3143 is 1.4×10^{42} erg s^{-1}. Calzetti et al. (2007) find the following relation between SFR in $M_\odot$ yr^{-1} and $L(24\ \mu{\rm m})$ in erg s^{-1},

$$SFR = 1.27 \times 10^{-24}[L(24\ \mu{\rm m})]^{0.885}.$$

Applying this to NGC 3143 gives SFR = 0.25 $M_\odot$ yr^{-1}. If the molecular gas depletion time of 2.2 Gyr from Leroy et al. (2013) applies to NGC 3143 as a whole, then a SFR of 0.25 $M_\odot$ yr^{-1} would require $M({\rm H}_2) = 5 \times 10^8$ $M_\odot$ about the same as its measured H I mass of 6.5×10^8 $M_\odot$. For a small galaxy it is unusual to have such a large fraction of the interstellar gas in molecular form.

2MASS K_s isophotes find that the isophotal major axis of NGC 3143 is at a position angle of 225°. Figure 18 reveals that H I emission extends about 50% farther on the northeastern major axis than on the southwestern major axis. At the lowest contour level [N(HI) $= 2.3 \times 10^{20}$ atoms cm^{-2}] in Figures 7 and 18, the semimajor axis of NGC 3143 is 31.5″ on the northeastern side and 20.5″ on the southwestern side, as if an interaction either truncated the H I disk on its southwestern side or elongated it on its northeastern side. At this contour level, the H I diameter of the major axis is 52″ $\pm$ 2″ for NGC 3143, 262″ $\pm$ 2″ for NGC 3145, and 122 $\pm$ 2″ for PGC 029578. The ratio of this diameter to D_{25} is 1.00 ± 0.17 for NGC 3143, 1.35 ± 0.09 for NGC 3145, and 1.20 ± 0.20 for PGC 029578.

The middle panel of Figure 18 displays all the channel maps of NGC 3143 with emission greater than 3 × the rms noise in Cube 3, the cube with 10.6 km s^{-1} velocity resolution. The location of the nucleus is marked by a cross. These channel maps indicate that the receding side is on the western side and the approaching side is on the eastern side.

In the bottom panel of Figure 18, contours from the first moment image of NGC 3143 from Cube 3 are overlaid on the N(HI) image in greyscale. Since the major axis diameter is only about 3 times the HPBW of the H I synthesized beam, we don't get much of a velocity field. Some estimates of the inclination i from the axis ratio are $i = 35°$ from 2MASS K_s isophotes and $i = 14°$ from the DSS image (Zaritsky et al. 1997). The value of the axis ratio from the N(HI) isophotes depends on whether we use the northeastern or the southwestern semimajor axis; with the northeastern semimajor axis we obtain $i = 35°$, whereas with the southwestern semimajor axis we get $i \leq 25°$. At the center of NGC 3143, the mean H I velocity = 3530 ± 5 km s^{-1}, which is consistent with the optical value of $v_{\rm sys} = 3536$ km s^{-1} from Schweizer (1987)
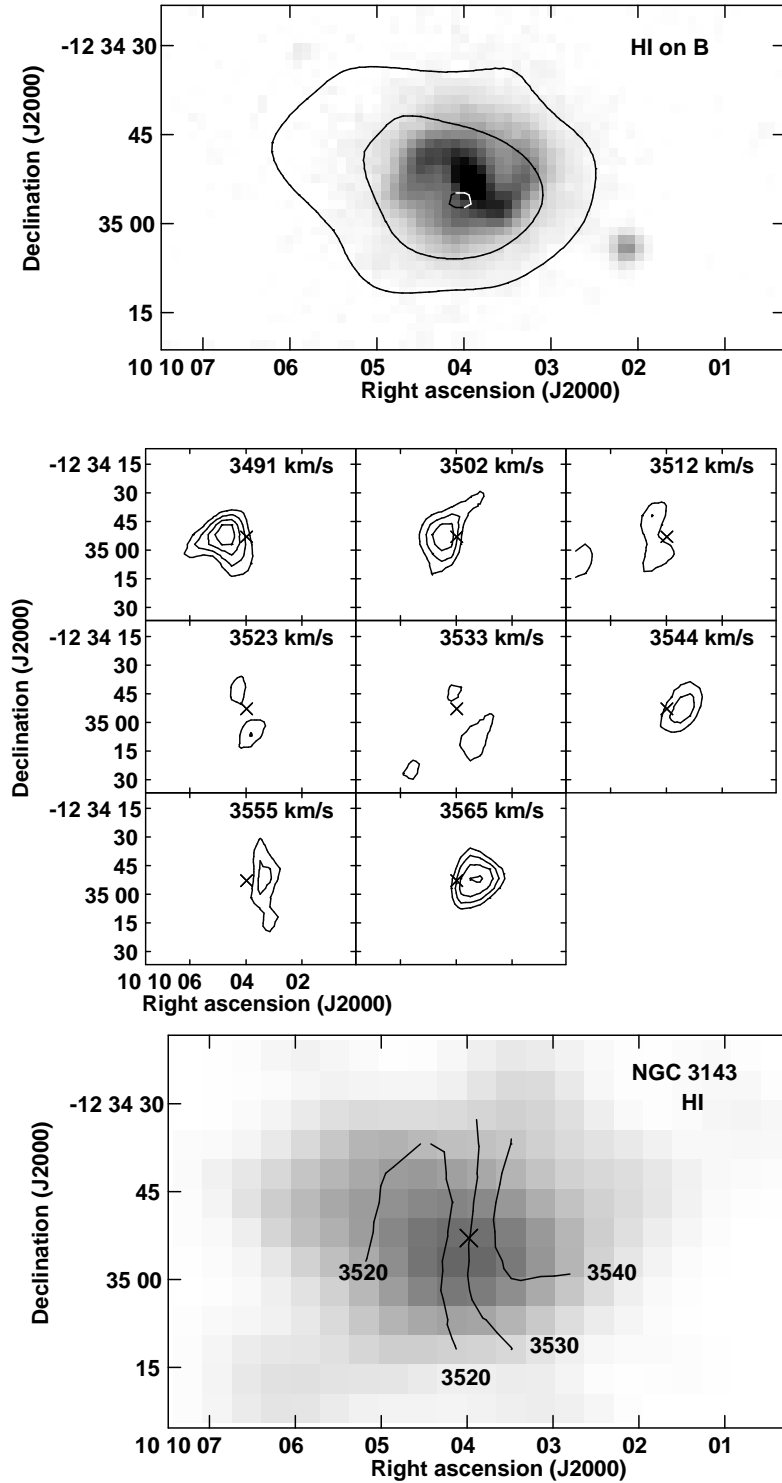
Figure 18. Top: $N(\mathrm{HI})$ contours of NGC 3143 overlaid on a B image in greyscale. Contour levels are at 100, 200, and 300 $\mathrm{Jy\,beam^{-1}}$ $\mathrm{m\,s^{-1}}$, where 100 $\mathrm{Jy\,beam^{-1}\,m\,s^{-1}}$ corresponds to $N(\mathrm{HI}) = 2.3 \times 10^{20}$ $\mathrm{atoms\,cm^{-2}}$. NGC 3143 is somewhat deficient in H I, and its H I emission is more elongated on the northeastern major axis than on the southwestern major axis. Middle: H I channel maps of NGC 3143 with contours at (3, 4, 5, 6) × the rms noise of 0.74 $\mathrm{mJy\,beam^{-1}}$ (equivalent to 1.0 K). Location of the nucleus is marked by a cross. The western side of NGC 3143 is the receding side. Bottom: Contours from the first moment map overlaid on the $N(\mathrm{HI})$ image in greyscale.
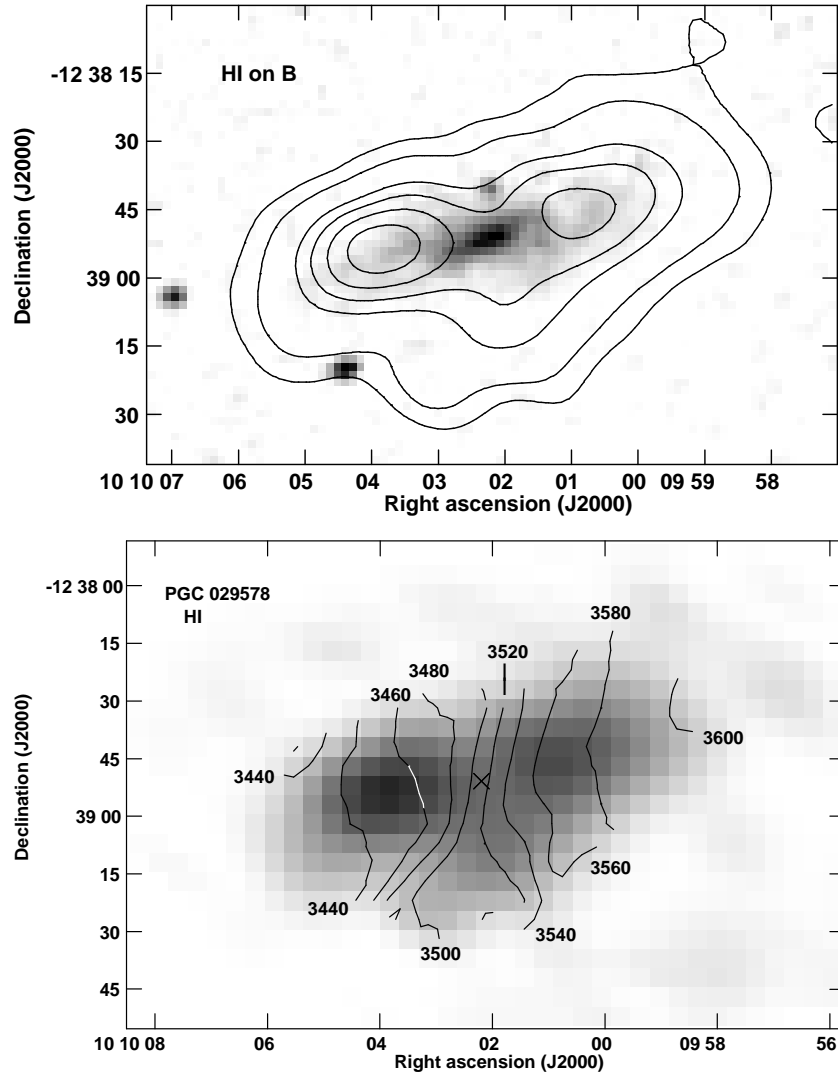
Figure 19. Images of PGC 029578. Top: N(HI) contours overlaid on a DSS image in greyscale. The contour levels are 100, 200, 400, 500, 600, 700, 800 Jy beam^{-1} m s^{-1}, where 100 Jy beam^{-1} m s^{-1} corresponds to N(HI) $= 2.3 \times 10^{20}$ atoms cm^{-2}. Bottom: Contours from the first moment image overlaid on the N(HI) image in greyscale, with a cross symbol marking the location of the nucleus.
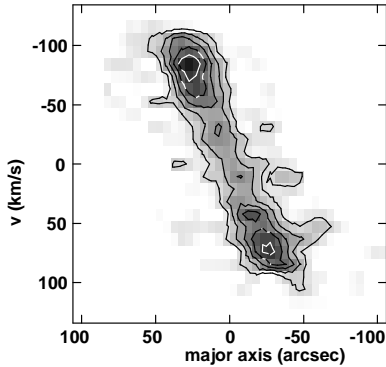
Figure 20. Position-velocity diagram of PGC 009578 along its kinematic major axis as a display of its rotation curve. Contours at $(2, 4, 6, 8, 10) \times$ rms noise of 0.74 mJy beam^{-1}, equivalent to 1.0 K.

and marginally consistent with the optical value 3506 ± 20 km s^{-1} at the nucleus measured by Zaritsky et al. (1997). Our H I value of $v_{\rm sys}$ for NGC 3143 is 125 ± 5 km s^{-1} below the value of $v_{\rm sys} = 3655.9 \pm 0.2$ km s^{-1} for NGC 3145. Therefore an encounter between these two galaxies could have had a significant component perpendicular to the disk of NGC 3145.

The value of $v_{sys} = 3652 \pm 5$ km s^{-1} listed on NED for NGC 3143 from Paturel et al. (2003) suffers from confusion with NGC 3145.

The other companion, the Sdm galaxy PGC 029578, is $12.97'$ $(= 204$ kpc$)$ south of NGC 3145. The H I mass of PGC 029578, 3.3×10^9 $M_\odot$, is 23% of M(HI) of NGC 3145 and five times the H I mass of NGC 3143.

The top panel in Figure 19 displays N(HI) contours of this galaxy overlaid on the DSS image in greyscale, and the bottom panel displays the velocity field contours from Cube 1 overlaid on the N(HI) image in greyscale. At the center of PGC 029578 the mean H I velocity is 3513 ± 5 km s^{-1}, which differs considerably from the long-slit optical value of 3586 ± 30 km s^{-1} for the nucleus obtained by Zaritsky et al. (1997). We wonder if the latter is a misprint. Our H I value of $v_{\rm sys}$ for PGC 029578 is 143 ± 5 km s^{-1} below that of NGC 3145. Thus an encounter between PGC 029578 and NGC 3145 could also have had a significant component perpendicular to the disk of NGC 3145.

Figure 20 displays the position-velocity (P-V) diagram of PGC 029578 along its kinematic major axis. Out to a radius R of $50''$ (i.e., approximately the optical semi-major axis $D_{25}/2$), the position angle of the kinematic major axis $= 270°$ on the receding side, and the rotation curve is symmetric. Beyond $R = 50''$, (i) the kinematic major axis on the receding side appears to align better with the isophotal major axis, which has a PA $= 283°$, and (ii) the velocity field on the approaching side becomes irregular.

Estimates of i are $68°$ from the optical axis ratio (see Table 1) and $61° \pm 2°$ from the H I axis ratio. At $R = 50'' = 13$ kpc, $(v - v_{\rm sys}) \sin i = 76$ km s^{-1}. Taking $i = 64° \pm 4°$ gives $v_{\rm rot} = 85 \pm 3$ km s^{-1}. Then for a spherically symmetric mass distribution, the dynamical mass $M_{\rm dyn} = 2.2 \times 10^{10}$ $M_\odot$. Out to the same radius $(R = 50'')$, the H I mass of PGC 029578 is 2.9×10^9 $M_\odot$, so M(HI)$/M_{\rm dyn} = 0.13$.

From the dynamical masses, the ratio of the mass of PGC 029578 to that of NGC 3145 is 0.044. From the K_s luminosities, the ratio of the stellar mass of NGC 3143 to that of NGC 3145 is 0.073. Thus the Sdm galaxy PGC 029578 has a lower mass than NGC 3143. PGC 029578 is also less luminous optically than NGC 3143 as it is 1.4 mag fainter in B and 1.6 mag fainter in R than NGC 3143 (see Table 1). However, as noted above, PGC 029578 has five times as much H I as NGC 3143. This is an indication that PGC 029578 has not experienced an encounter recently since otherwise its H I content would be lower as a result of gas loss and/or enhanced star formation.

It is more likely that NGC 3143 was involved in a recent interaction because its SFR seems to be enhanced, its H I emission is 50% more extended on its northeastern side, it is somewhat deficient in H I, and it appears to have a large molecular fraction.

The simple analytic model in the Appendix demonstrates that an encounter between NGC 3143 and NGC 3145 could have triggered the observed warping mode in NGC 3145. It illustrates some of the considerations necessary for making a detailed numerical model. The latter is beyond the scope of this paper. The observed anti-symmetric warping motions in NGC 3145 (see Section 4.2.1) have line-of-sight magnitude ~ 40 km s^{-1} (or $v_z \sim 60$ km s^{-1} if the observed motions are completely perpendicular to the disk). In the model, the magnitude Δv_z of the warping motions and the maximum displacement Δz of the material above the plane of the disk depend on how shallow the attack angle of the companion's trajectory is relative to the disk of NGC 3145. For a particular choice of orbital tilt angle, this analytic model creates warping motions in NGC 3145 of magnitude ~ 200 km s^{-1}, with NGC 3143 pulling up on one side of the disk of NGC 3145 and down on the opposite side of the disk. These would warp the disk by ~ 5 kpc. Given the assumptions in the model, these values of Δv_z and Δz are uncertain by a factor of a few. A slightly steeper angle of attack with the same flyby velocity would give a more modest warp. The comparison in the Appendix between the time elapsed since closest approach and rough estimates of the period of vertical oscillation of the warp suggests that the warp material may have experienced about one vertical oscillation. Thus the extra-planar features produced by this encounter should still be present.

6. DISCUSSION AND CONCLUSIONS

NGC 3145 is a spiral galaxy with several optical peculiarities. For example on the southern side of NGC 3145, stellar arms cross, forming "X"-features, and outline an apparent triangular region. Sandage's peculiar arm forms the eastern edge of the *triangle*. As this arm heads southwest from the inner disk of NGC 3145, it crosses first a string of blue clumps, then an inner spiral arm at the eastern apex of the *triangle*, and then another stellar arm at the southern apex of the *triangle*.

Together with its two smaller companions, NGC 3145 forms the NGC 3145 triplet. To study the above features and other optical anomalies, we analyzed VLA H I observations of this group and VLA $\lambda 6$ cm radio continuum observations of NGC 3145.

Our $\lambda 6$ cm radio continuum observations yield the following information about NGC 3145

(1) Lack of prominent radio continuum emission at the eastern and southern apices of the *triangle* rules out shock fronts at the arm-crossing "X"'s there. This means that the arms appearing to cross at these locations must be in different planes and that the portion of Sandage's peculiar arm outlining the eastern edge of the *triangle* is not in the disk.

(2) North of the *triangle*, there is extended radio continuum emission along Sandage's peculiar arm. This is indicative of shocked gas. Hence this portion of Sandage's peculiar arm, which includes where it crosses the string of blue clumps, appears to be in the disk. The suggestion is that Sandage's peculiar arm emerges from the disk before it reaches the *triangle*.

Our H I observations find the following kinematic anomalies in NGC 3145.

(1) In large areas of NGC 3145, the line-profiles are skewed. In the middle-to-outer part of the gas disk, line-profiles near the major axis consist of a large amplitude peak plus a broader, skewed wing. Relative to the disk, the gas in the skewed wing has z-motions away from us on the approaching side of the galaxy and z-motions towards us on the receding side. The difference $v_2 - v_1$ between the central velocity of the skewed wing and that of the large amplitude peak has a mean value 37 ± 3 km s^{-1} on the approaching side and -47 ± 7 km s^{-1} on the receding side. This kinematic anti-symmetry implies that there has been a perturbation with a sizeable component perpendicular to the disk over large spatial scales, e.g., the disk is undergoing a warping as a result of a close passage by one of its companions. We detect these warping motions out to a radius of at least $105'' = 28$ kpc.

(2) There are two features whose velocities imply that they are out-of-plane tidal arms. One is the apparent branch of the main spiral arm on the northeastern side of the galaxy. Where the *branch* and the main spiral arm appear to intersect in projection, the *branch* has a line-of-sight velocity ~ 150 km s^{-1} greater than that of the main spiral arm. We conclude that the *branch* is an out-of-plane tidal arm and may have streaming motions along it. The other is Sandage's peculiar arm as line-profiles of the western-antenna extension of Sandage's peculiar arm exhibit two clearly distinct peaks of comparable amplitude separated by 56 km s^{-1} in line-of-sight velocity. We attribute one of these to H I in the disk and the other to H I in Sandage's peculiar arm, which thus appears to be another tidal arm. These arms appear relatively short for tidal arms; more sensitive H I observations are necessary to see if these tidal arms extend farther.

(3) The distribution of H I emission from NGC 3145 is not axisymmetric: within the main optical disk there are massive H I concentrations NW, NE, and SW of the nucleus and a trough on the SE side. This peculiarity is other evidence of an encounter.

Our observations solve the puzzle of Sandage's peculiar arm, i.e., it is a tidal arm tilted with respect to the plane of the disk of NGC 3145, and this tidal arm emerges from the disk before it reaches the apparent arm crossings at the *triangle*. Furthermore, our H I observations revealed anti-symmetric warping motions in NGC 3145 on large spatial scales out to 28 kpc. The two relatively-short, extra-planar tidal arms are evidence that NGC 3145 has recently experienced a combination of azimuthal and perpendicular perturbations. The warping motions are evidence that it has recently experienced a perpendicular perturbation affecting the middle-to-outer part of the gas disk.

The Sdm galaxy PGC 02978 shows no evidence of having undergone an encounter recently, whereas NGC 3143 has an enhanced SFR, somewhat of an H I deficiency compared to its SFR, H I emission 50% more extended on its northeastern side than on the opposite side, and an apparently large molecular fraction for a small galaxy. Thus NGC 3143 is the more likely of the two companions to have interacted with NGC 3145.

Our simple analytic model demonstrates that an encounter between NGC 3143 and NGC 3145 is a plausible explanation for the observed warping motions in NGC 3145.

APPENDIX

ANALYTIC PLAUSIBILITY MODELS FOR THE COLLISION

Although the observations of the NGC 3145 system may not appear sufficient to constrain narrowly the parameters of the collision that likely produced the anomalous disk structure of NGC 3145, one factor gives considerable leverage: the companions are far from the primary i.e., more than a few primary diameters. It is possible that the relative orbit

is hyperbolic. Yet a second fact, that the mass ratio is evidently less than 10%, makes that unlikely. A hyperbolic encounter with a low mass companion will not have much effect. A slightly bound orbit is more likely. In either case, the effects of dynamical friction are probably minimal.

We assume that the relative orbit is marginally bound and, based on the arguments in Section 5, that NGC 3143 is the collision companion. We use its observed properties: plane-of-sky distance from NGC 3145 = 140 kpc and line-of-sight relative velocity= 125 km s^{-1}. The rotation curve of NGC 3145 is relatively flat beyond 13 kpc, so we can make the further simplifying assumption that the dark-halo density profile (and logarithmic potential) is the same all the way out to the companion. In that case the orbital shape will be well described by the p-ellipse approximation of Struck (2006, 2015), especially by Figs. 6-8 of the latter paper. Even though we do not know the angular orientations of the orbit, knowing its shape is helpful. For example, a very radial p-ellipse in this potential is significantly curved only near its maximum and minimum radii, and is nearly straight otherwise. This, in turn, tells us that unless the companion is at its maximum radius (apoapse), its direction of motion has changed little since it left the vicinity of the primary. This means that the trajectory has not curved or bowed out into the E-W direction, but lies mostly in the plane containing the N-S line, and perpendicular to the sky.

Two interrelated questions remain: 1) what is the angle of the companion's trajectory relative to the plane of the sky and, 2) how close is the companion to apoapse? Given the large visible separation between the two galaxies, and the fact that particles on very radial orbits spend most of their time near apoapse, it seems reasonable to suppose that the companion is indeed near apoapse. The following energy equation provides a constraint,

$$\frac{1}{2}v_1{}^2 = -\frac{GM_1}{r_1}ln\left[\frac{r_1}{r_{\max}}\right], \tag{A1}$$

where v_1 is the current relative velocity of the companion, so the left-hand side of the equation is the specific kinetic energy. The right-hand side is the potential energy difference between the current radius r_1 and the apoapse radius $r_{\max}$. Here M_1 is the mass contained within the radius r_1. Specifically,

$$M_1 = M_o\left(\frac{r_1}{r_o}\right), \tag{A2}$$

where the 'o' subscript refers to values at the radius of NGC 3145 beyond which the trajectory of the companion is assumed to be nearly straight until it reaches apoapse. From Table 4 we take $r_o = 33$ kpc and $M_o = 5 \times 10^{11} M_\odot$.

Equation A1 can be solved for the radius ratio, and with equation A2 we have,

$$ln\left[\frac{r_1}{r_{\max}}\right] = \frac{-r_1 v_1{}^2}{2GM_1} = -0.12\left(\frac{r_o}{33\text{ kpc}}\right)\left(\frac{v_1}{125\text{ km s}^{-1}}\right)^2\left(\frac{5\times10^{11}\ M_\odot}{M_o}\right)(\sin\theta)^{-2}, \tag{A3}$$

where the sine term accounts for the angle between the trajectory and the plane of the sky, and the fact that we observe the velocity component perpendicular to it. For example, if we choose $\theta = 45°$, then $r_1 = (140\text{ kpc})/\cos(45°)$ = 200 kpc, $v_1 = (125$ km s$^{-1})/\sin(45°)$ = 177 km s^{-1}, and the radius ratio is 0.79. This value for the radius ratio is consistent with the assumption that the companion is near apoapse.

Then we can use the energy equation again to estimate the velocity at r_o, which is near closest approach. i.e.,

$$v_o{}^2 = \left(177\text{ km s}^{-1}\right)^2 + \frac{2GM_o}{r_o}ln\left[\frac{r_1}{r_o}\right]. \tag{A4}$$

This example calculation gives $v_o = 515$ km s^{-1}, which seems reasonable.

We do not know the angle of attack of the companion trajectory relative to the NGC 3145 disk. However, given that the disk does not have a strong ring, the impact was unlikely to be perpendicular. NGC 3145 has two features that are extra-planar tidal arms, one in the northeast and the other in the south to southwest, and neither is a prominent, long tidal tail. Therefore the impact was unlikely to be planar. The combination of the two stubby, out-of-plane tidal arms (evidence for azimuthal and perpendicular perturbations) and the global warp suggests an intermediate angle of attack.

With estimates for the maximum radius of about 250 kpc, and the minimum radius of about 15 kpc, we can use the p-ellipse approximate equation to estimate the p-ellipse eccentricity in this potential,

$$\frac{r_{max}}{r_{min}} = \left(\frac{1+e}{1-e}\right)^{1/2}. \tag{A5}$$

This yields $e = 0.993$. The formulae of Struck (2006, 2015), suggest that such an orbit will turn through an angle of about 125° near closest approach. Thus, we can envision its closest approach arc as roughly semi-circular ($\pm60°$ on either side of the impact point), with a radius of about 15 kpc and a fairly shallow angle of impact. At the ends of this arc the companion is about one radius length above or below (different sectors of) the disk. On the incoming end it will pull up. On the outgoing end it will pull down.

Assume the companion pulls on each of these disk sectors for a time roughly equal to the time it takes to traverse half the curved arc, i.e., a time about equal to about $(15 \text{ kpc}/470 \text{ km s}^{-1}) \simeq 32$ Myr. Then, the vertical velocity impulse felt by that sector is about,

$$\Delta v_z = a_{comp}\Delta t \simeq \frac{GM_{comp}\Delta t}{\left(\frac{r_{\min}}{3}\right)^2} \simeq 200 \text{ km s}^{-1}, \tag{A6}$$

where the companion mass has been assumed to be about $3.7 \times 10^{10} M_\odot$, and it is assumed that the mean vertical acceleration occurs when the companion is at a z distance equal to about $1/3$ of r_{min}, i.e., a moderately shallow angle of attack relative to the disk plane.

Assuming that this impulse is countered by the vertical component of the halo potential, material in this sector will rise to a height of about,

$$\Delta z \simeq \frac{\Delta v_z^2}{\left(\frac{2GM(r_{min})}{r_{min}^2}\right)} \simeq 5.0 \text{ kpc}. \tag{A7}$$

This shows that it is plausible that the encounter has warped the disk of NGC 3145 by at least several kpc. At the given flyby velocity, a slightly steeper angle than that assumed in eq. (A6) would give a more modest warp, while a shallower angle would give an even stronger warp. If the flyby velocity was much greater, then the material would not be lifted to kpc levels. If the flyby velocity was much lower, with the moderate angle of attack, longer tails would be produced.

There are also some timescale constraints, for example, how does the time since closest encounter compare to the oscillation time of the warp? If the latter is much shorter than the former, we might expect the warp to have smoothed away by the present. As an estimate for the former we can use the half period of the adopted p-ellipse orbit. This period is given by eq. (C4) in Appendix C of Struck (2006) (with a small error corrected). In the present notation, the half-period can be written as,

$$T_{1/2} = 1.1 \left(\frac{5 \times 10^{11} \ M_\odot}{M_o}\right) \left(\frac{r_o}{33 \text{ kpc}}\right) \left(\frac{a}{132 \text{ kpc}}\right)^2 \text{ Gyr} \tag{A8}$$

where a is the semi-major axis of the orbit $((15 + 250)/2 = 132 \text{ kpc})$. This value is also the same as the free-fall time onto the galaxy center with the assumed parameters.

The oscillation time can be estimated by the vertical epicyclic frequency of the disk. Since most of the warp is relatively far out in the disk, we assume that the local gravity of the disk there is negligible and the restoring force is provided by the vertical component of the total gravity interior to that radius. This approximation seems especially appropriate for a large warp involving most of the local disk material. Then we can approximate the vertical restoring gravitational acceleration as,

$$g_z = -\frac{\partial \Phi}{\partial z} \simeq -\frac{GM(r)}{r^2}\frac{z}{r}. \tag{A9}$$

The vertical epicyclic frequency is defined by,

$$\nu^2 = \frac{\partial^2 \Phi}{\partial z^2} \simeq \frac{GM(r)}{r^2 + z^2} \simeq \frac{GM(r)}{r^2}. \tag{A10}$$

Assuming a nearly flat rotation curve, we approximate $M(r = 15 \text{ kpc})$ as about half M_o, and obtain the following estimate of the vertical epicyclic period,

$$\tau = \frac{2\pi}{\nu} \simeq 352 \text{ Myr}. \tag{A11}$$

Taken at face value the comparison of eqs. (A8) and (A11) suggest that the warp has gone through a few epicyclic oscillations by the present. This is possible, but it is more likely that the oscillation period is considerably longer. The first reason for this is that the epicyclic approximation assumes a very small excursion. Since the estimate of eq. (A7) yields a fairly large excursion, the true nonlinear oscillation period is likely much longer. The second reason is that once the material in the warp moves out of the disk plane it will not be centripetally balanced in the radial direction. Its true motion (even in an azimuthally co-rotating frame) will be a combination of nonlinear vertical and radial oscillations. This will introduce another significant increase in the overall period. Thus, it is likely that the vertical epicyclic timescale should be increased by a factor of a few, and the warp material has experienced about one oscillation.

These timescale considerations further constrain the putative encounter, and especially the angle-of-attack. In sum, if NGC 3143 is indeed the collision companion, then the structure of the encounter is quite constrained.

REFERENCES

Banfi, M., Rampazzo, R., Chincarini, G., & Henry, R.B.C. 1993, A&A, 280, 373

Brandt, J.C. 1960, ApJ, 131, 293

Calzetti, D., Kennicutt, R.C., Engelbracht, C.W., et al. 2007, ApJ, 666, 870

Condon, J.J. 1992, ARA&A, 30, 575

Condon, J.J., Cotton, W.D., Greisen, E.W., Yin, Q.F., Perley, R.A., Taylor, G.B., & Broderick, J.J. 1998, ApJ, 115, 1693

de Vaucouleurs, G., de Vaucouleurs, A., Corwin, H.G., Jr., Buta, R.J., Paturel, G., & Fouqué, P. 1991, Third Reference Catalogue of
    Bright Galaxies (New York: Springer)

Doyle, M.T., Drinkwater, M.J., Rohde, D.J., et al. 2005, MNRAS, 361, 34

Elmegreen, D.M., Kaufman, M., Brinks, E., Elmegreen, B. G., & Sundin, M. 1995, ApJ, 453, 100

Faber, S.M. & Gallagher, J.S. 1979, ARA&A, 17, 135

Kamphuis, J. J. 1993, Ph.D. thesis, Groningen University

Kaufman, M., Brinks, E., Elmegreen, D.M., Thomasson, M., Elmegreen, B.G., Struck, C., & Klariç, M. 1997, AJ, 114, 2323

Kaufman, M., Brinks, E., Elmegreen, B.G., Elmegreen, D.M., Klariç, M., Struck, C., Thomasson, M., & Vogel, S. 1999, AJ, 118, 1577

Kim, W.-T. & Ostriker, E.C. 2002, ApJ, 570, 132

Kim, W.-T. & Ostriker, E.C. 2006, ApJ, 646, 213

La Vigne, M.A., Vogel, S.N., & Ostriker, E.C. 2006, ApJ, 650, 818

Lee, W.-K. & Shu, F.H. 2012, ApJ, 756, 45

Lee, W.-K. 2014, ApJ, 792, 122

Leroy, A.K., Walter, F., Sandstrom, K., et al. 2013, AJ, 146, 19

Martini, P., Regan, M., Mulchaey, J., & Pogge, R. 2003, ApJS, 146, 353

Paturel, G., Theureau, G., Bottinelli, L., Gouguenheim, L., Coudreau-Durand, N., Hallet, N., & Petit, C. 2003, A&A, 412, 57

Persic, M. & Salucci, P. 1991, ApJ, 368, 60

Robert, M.S. & Hayes, M.P. 1994, ARA&A, 32, 115

Rubin, V.C., Ford, W.K., & Thonnard, N. 1978, ApJ, 225, L107

Rubin, V.C., Ford, W.K., Jr., Thonnard, N. & Burstein, D. 1982, ApJ, 261, 439

Sandage, A. 1961, The Hubble Atlas of Galaxies, Carnegie Institution of Washington (Washington, D.C.), Publ. 618

Sandage, A. & Bedke, J. 1994, The Carnegie Atlas of Galaxies, Vol. II, Carnegie Institution of Washington (Washington, D.C.)

Schweizer, L.Y. 1987, ApJS, 64, 411

Shetty, R. & Ostriker, E.C. 2006, ApJ, 647, 997

Skrutskie, M.F., Cutri, R.M., Stiening, R., et al. 2006, AJ, 131, 1163

Struck-Marcell, C. 1990, AJ, 99, 71

Struck C. 2006, AJ, 131, 1347

Struck C. 2015, MNRAS, 446, 3139

Zaritsky, D., Smith, R., Frenk, C., & White, S.D.M. 1997, ApJ, 478, 39